Numerical analysis of wave-induced forces on storm surge barrier sector gates

V.I. Renkema

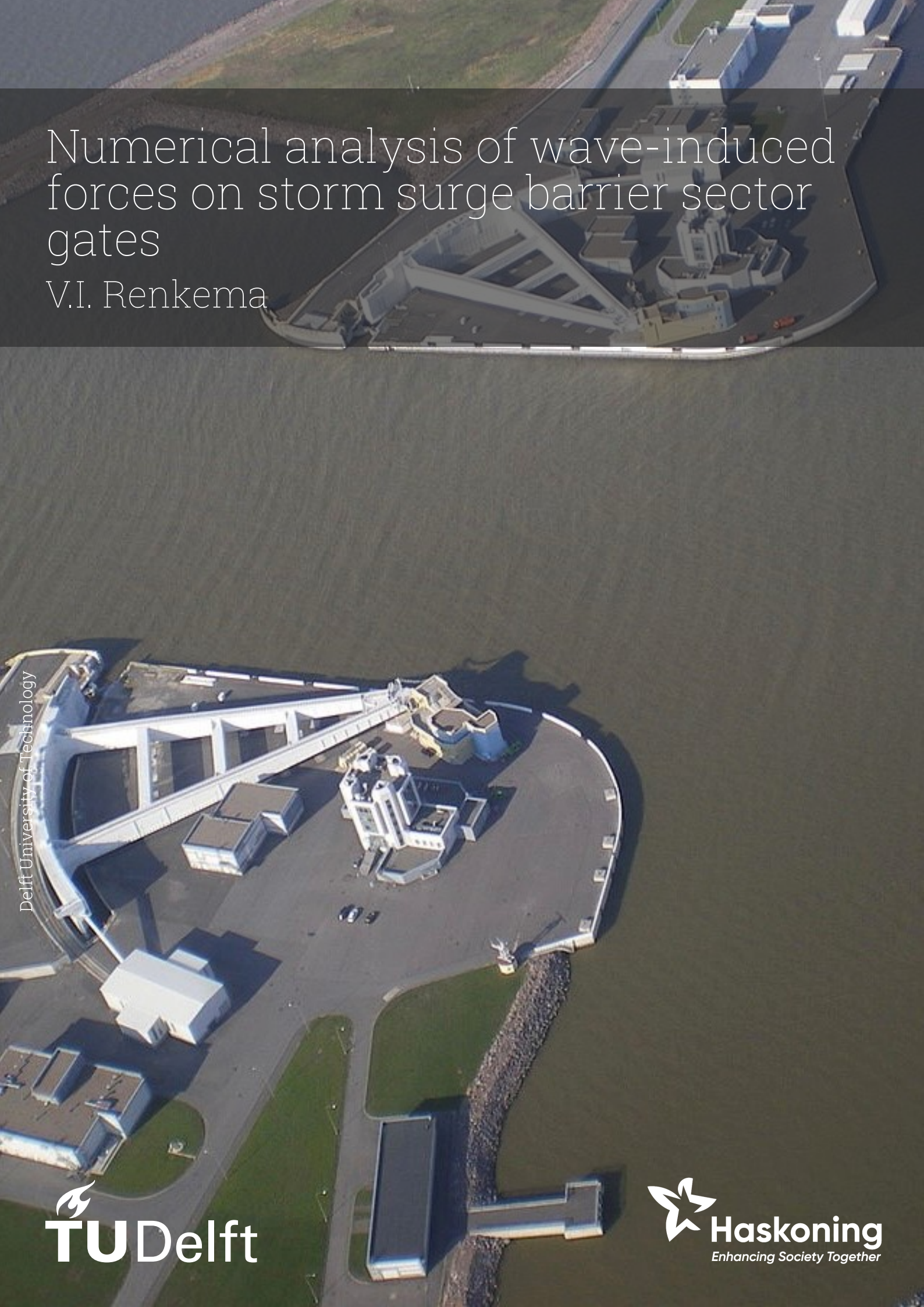

Delft University of Technology

TU Delft

Haskoning
Enhancing Society Together

Numerical analysis of wave-induced forces on storm surge barrier sector gates

by

V.I. Renkema

in partial fulfilment of the requirements for the degree of

Master of Science

in Civil Engineering

at the Delft University of Technology,

Committee Chair:	Dr. ir. A. Antonini,	TU Delft
Committee members:	Dr. ir. B. Hofland,	TU Delft
	Prof.dr.ir. S.N. Jonkman,	TU Delft
	Ir. M. Horstman,	Haskoning
	Ir. M. Sokolewicz,	Haskoning

Cover photo: by Sergei S. Rublev

TU Delft

Haskoning
Enhancing Society Together

Preface

This research marks the last stage of obtaining the master degree in Civil Engineering. The process of working with CFD modelling has challenged me many times, but it was also a very exciting and educational experience.

I would like to thank Haskoning for their collaboration on this study and for providing many learning opportunities, resources and internal expertise that greatly supported the successful completion of this study. I am especially thankful to everyone at Haskoning who offered advice and shared knowledge through this project.

I would like to express my sincere gratitude to the chairman of the graduation committee, Alessandro Antonini, for his guidance through the entire process and his willingness to schedule meetings to discuss the ideas and challenges of CFD modelling. His expertise in this field has helped me a lot in understanding such a challenging topic. I am also grateful to Bas Hofland, whose guidance has helped me a lot to develop critical thinking about the modelling and deepen my understanding of the theoretical principles behind wave-structure interactions. Furthermore, I would like to thank Bas Jonkman for showing great interest in my work, offering valuable feedback and suggestions that have enriched this study.

I would like to sincerely thank Marc Horstman and Marius Sokolewicz for welcoming me to Haskoning. I am especially thankful to Marc Horstman for his guidance and support through this study. His expertise in CFD modelling has helped me a lot in solving many challenges while working on my thesis.

V.I. Renkema
Delft, July 2025

Abstract

The increasing magnitude and frequency of storms driven by climate change have increased global demand for flood protection barriers. Sector gates are one of the barrier types, providing storm surge protection while letting marine traffic pass during normal conditions. However, no dedicated design guidelines currently exist for these structures, and the uniqueness and large scale of sector gates often make conventional design methods suboptimal.

This research investigates a method for determining wave-induced forces on sector gates using three-dimensional computational fluid dynamics (CFD) modelling with OpenFOAM and the Waves2Foam package. Accurate prediction of wave pressure distributions is essential for optimising sector gate design, and CFD offers a high resolution, which is an alternative to traditional physical and empirical approaches. The goal of this study is to evaluate the capability of 3D CFD modelling to analyse the spatial and temporal distribution of wave loads on complex geometries such as sector gates.

The St. Petersburg storm surge barrier was used as a case study. Two 2DV OpenFOAM models, based on Goda's experiments and the St. Petersburg case study, were developed. A 3D model for the St. Petersburg case study was then developed based on these results. The 2DV results showed good agreement with physical test data and confirmed that empirical methods tend to overestimate forces. It was further observed that maximum pressure occurs prior to the peak water elevation at the structure.

The 3D CFD model was simulated under a regular, non-oblique incident wave condition. Due to computational constraints, the model domain was limited to a single gate with a resolution of 12 cells per wave height. The maximum horizontal force obtained from the CFD model was 16.7 MN, falling within the range of 12.2 MN to 17 MN measured in physical model tests. However, minimum force predictions were approximately 50% lower than expected. The model identified critical loading areas, notably, at the junction between gates and at approximately two-thirds of the gate curvature from the junction point. Additionally, a node-antinode pattern in wave pressure along the barrier wall was observed, with extracted phase differences relative to the antinode at the junction between gates, providing further insight.

While significant computational resources are required, as the 3D CFD model took 2.5 weeks to simulate 250 seconds, the results demonstrate this method enhances understanding of wave-structure interactions under extreme conditions. It can be used to complement physical model testing in the detailed refinement phase of the design process.

Contents

Symbols & Abbreviations

Abbreviations

Abbreviation	Definition
CFD	Computational Fluid Dynamics
OCW3D	OceanWave3D
OpenFOAM	Open Field Operation And Manipulation
SWL	Still Water Level
VOF	Volume of Fluid
WG	Wave Gauge

Symbols

Symbol	Definition	Unit
A	Wave amplitude	[m]
F	Force	[N]
H	Wave height	[m]
L	Wavelength	[m]
T	Wave period	[s]
U	Velocity	[m/s]
d	Water depth	[m]
g	Gravity	$[m/s^2]$
h	Wave height	[m]
k	Wave number	$[m^{-1})]$
n	Total number of data points	[-]
p	Pressure	$[N/m^2]$
p_s	Hydrostatic pressure	$[N/m^2]$
t	Time	[s]
α	Phase fraction coefficient	[-]
η	Water surface elevation	[m]
ρ	Density of water	$[kg/m^3]$

1

Introduction

For the past years, human activity has led to concerns regarding its effect on the climate. The changing climate will likely increase the magnitude and frequency of extreme hydrodynamic conditions, such as storm surges (Ahmed et al., 2022). This could make coastal zones more vulnerable to floods, which means there is a higher demand for coastal protection measures worldwide. Governments are expected to invest in such measures (Mooyaart et al., 2014).

The already existing coastal protection measures, such as movable storm surge barriers, have proven to be effective against severe weather conditions. These structures allow marine traffic to pass under normal conditions and provide a barrier against elevated water levels during storms (Walraven et al., 2022b). Storm surge barriers that consist of two circular segments and transfer forces through a steel frame are called sector gates (Mooyaart et al., 2014). Figure 1.1 shows an example of such a structure.

Sector gates have a horizontal rotation axis. When the gates have a vertical rotation axis, they are classified as segment gates. Compared to segment gates, sector gates primarily cover the channel width, whereas segment gates primarily cover the depth of the water. This makes sector gates typically larger and more unique.

Figure 1.1: The Maeslant Barrier, Netherlands (Rijkswaterstaat, n.d.)

The primary challenge in designing a storm surge sector gate barrier is its uniqueness since each is designed for a specific environment and environmental conditions (Walraven et al., 2022b). For this reason, there is a lack of standardized design guidelines for such structures. In addition, the circular shape of the gates complicates the calculation of hydraulic forces.

1.1. Problem statement

In the year 2022, only 18 storm surge barriers were reported to exist worldwide (Vader et al., 2023). Given the limited number of constructed storm surge barriers and the wide range of highly variable hydraulic conditions, various unique gate types can be implemented. This explains why most existing storm surge barriers are considered prototypes (Walraven et al., 2022a). In addition, sector gate structures were constructed on a large scale only in Russia (St. Petersburg flood protection barrier) and the Netherlands (Maeslant Barrier). The design of these structures was primarily based on forces calculated from empirical relations and laboratory tests for such storm surge barriers in the past. These methods are time-consuming and expensive. As the demand for storm surge barriers increases, for example, a similar structure is being considered for construction in the Houston Galveston Bay region (USACE, 2021), there is a growing need for more efficient testing and understanding of loads on barrier gates. Furthermore, as no universally optimal gate type exists, a custom-made design is needed for a certain location's operational and environmental requirements (Dircke et al., 2012). There are no design guidelines for storm surge barriers, unlike developed design guidelines for dams, dikes, and breakwaters (Mooyaart et al., 2014).

Liang et al. (2024) conducted research on the performance of sector gates. The focus of the study was on the static performance of ship lock sector gates, which are similar to the storm surge barrier sector gates. This research emphasizes the significance of spatial stress characteristics, as sector gates are subjected to bidirectional hydraulic heads, self-weight, and other complex loads. Furthermore, Liang et al. (2024) highlighted a lack of existing research regarding the performance of sector gates, indicating a research gap.

Mooyaart et al. (2014) gives an overview of types of storm surge barriers, a function overview, and a cost overview. However, no exact design guidelines for storm surge barriers have been documented. According to Stagonas et al. (2014), there is limited knowledge on pressures and loads induced by waves, and mainly referred to structures like parapets and piers. As a result, this study has focused on mapping wave-induced pressures on wave recurves. It showed that there is a significant spatial variation of wave-induced pressures. This pertains to an additional confinement effect due to the shape of the sector gate.

According to Ravindar et al. (2016), knowing the impact of wave pressure and its distribution on the structure is of great importance for economical and stable design. When interacting with a structure, the waves during extreme conditions exert high-impact loads on it, which may lead to structural failures (Ravindar et al., 2016). Furthermore, this study observes that the wave-induced pressure on a structure exhibits significant spatial and temporal variability within each individual wave cycle. Accurately resolving the spatial distribution of these pressures remains challenging when using conventional point-based pressure transducers. Ravindar et al. (2016) attempted to obtain spatial pressure distribution on curve-shaped wave parapets. However, a notable limitation of the experimental methodologies employed was the low sampling rate.

Therefore, it is evident that understanding the wave pressure distribution on a structure is essential; however, experimental studies are restricted by sampling limitations. Such limitations can be overcome using Computational Fluid Dynamics (CFD) modeling. According to Mingham et al. (2016), the advantages of CFD modeling include the ability to obtain data at any points of interest in the domain. CFD models have lower set-up costs, are not challenged by scaling effects, and geometry and wave conditions are easily adjustable. However, this study mentions such limitations as long run times, the chance of having an inappropriate model setup that leads to incorrect physics, and possible errors due to approximation algorithms.

The majority of computational fluid dynamics (CFD) models analyzed to date are two-dimensional vertical (2DV) models, which resolve flow and processes within a vertical plane. While 2DV models effectively capture vertical and longitudinal domains, they inherently neglect lateral variations within the computational domain and are therefore unable to account for phenomena such as wave refraction, diffraction, and three-dimensional wave-structure interactions. Consequently, when laterally varying or geometrically complex wave-structure interaction problems must be addressed, fully three-dimensional (3D) modeling becomes necessary. However, the incorporation of the third spatial dimension increases computational costs and demands greater computational power and memory resources. Furthermore, the capability of existing 3D CFD models remains only partially validated. Although wave-structure interactions have been extensively investigated within the 2DV framework, these models are unsuitable for simulating scenarios involving significant lateral hydrodynamic effects and standing wave formation across the channel width.

Additionally, introducing the third direction into a model means that wave reflections are not confined to a single direction, unlike the two-dimensional cases. In the case of sector gates, the spatially varying wave reflection patterns observed on the seaward side of the gates, as illustrated in Figure 1.1, demonstrate pronounced lateral variations. These complex reflection patterns cannot be resolved within the limitations of 2DV models, which inherently neglect lateral spatial variability in the computational domain.

In general, the role of reflection in the three-dimensional CFD model has not yet been studied. However, the addition of the third dimension is considered to provide a more accurate representation of the forces exerted on the structure.

1.2. Research questions

This research uses the OpenFOAM (specifically, the CoastalFOAM package) CFD model for analysis of wave-structure interaction. Specifically, the study focuses on the validation of the three-dimensional model against the laboratory experimental data. As a final result, a significant wave load pressure distribution is determined and mapped as part of this research. The CFD model is being validated based on the St. Petersburg flood protection barrier case, the design of which was evaluated in the laboratory experiments in 2009. The results from the model are compared to laboratory data by analyzing patterns of forcing behavior and comparing force magnitudes.

This research addresses the following research question:

How can 3D Computational Fluid Dynamics (CFD) modeling be utilized in order to analyze the spatial distribution of wave-induced pressure on storm surge sector gates?

In order to answer the research question, first, the following sub-questions will be answered:

- How does the CFD model perform compared to the forces measured during the experimental study?
- What is the design pressure distribution on the sector gate?
- What are the critical points of pressure in the gate during extreme conditions?

1.3. Methodology outline

In this study, a computational fluid dynamics (CFD) model is employed to investigate the spatial and temporal variability of wave-induced pressure. To facilitate this analysis, the methodology is structured into five stages, after which conclusions are drawn, as shown in Figure 1.2

In step 1, the case study was analyzed. In step 2, a literature study was conducted, primarily focusing on wave-structure interaction, wave-induced pressure, forces on the walls, and numerical modeling. Based on the literature study and case study analysis, in step 3, the boundary conditions, grid resolution, and hydraulic conditions were defined for both 2DV and 3D cases.

In step 4, before applying these models to the case study, the 2DV CFD model was validated by using Goda's 1966 experiment data. The hydraulic conditions from the physical experiment were replicated in the numerical model, and the simulation results were subsequently compared to the experimental measurements.

After validating the 2DV model using Goda's experiments, the results were obtained from the 2DV model based on the case study. These results were compared with empirical relationships that are commonly used as a reference in design processes of hydraulic structures and Linear Wave Theory. Based on the 2DV case, a 3D case was set up. The 3D numerical results were compared to the physical model results.

Lastly, in step 5, the pressure time series of the 3D model was used to draw conclusions about the temporal and spatial distribution of pressure on the sector gate.

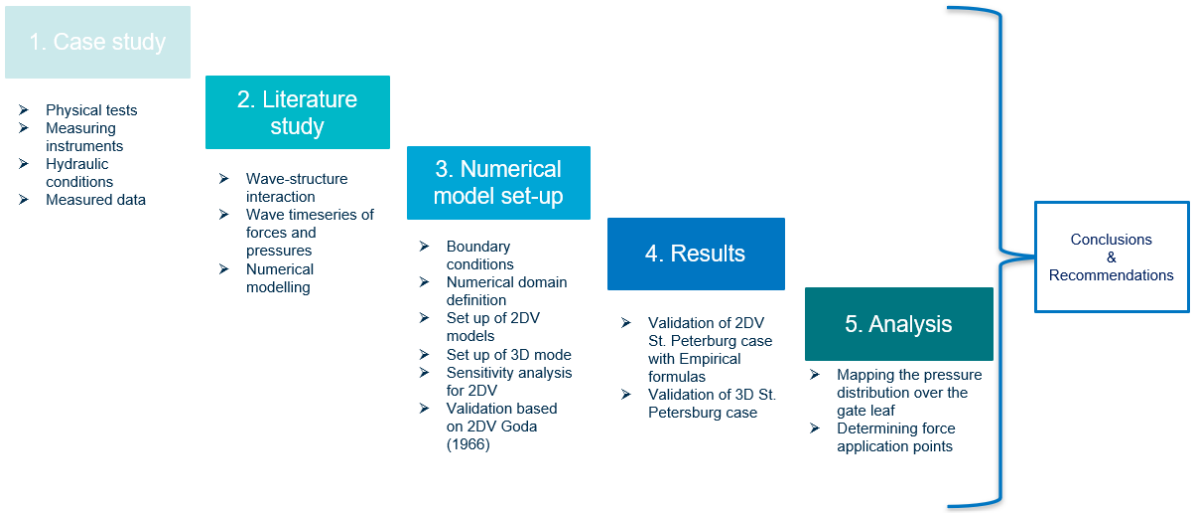

Figure 1.2: Methodology outline

1.4. Thesis outline

This MSc thesis uses the following approach, which is reported in the following structure:

- **Chapter 1** outlines the relevance of this study to the community, describes the research that was done related to the study, and the importance of filling the existing research gap. Subsequently, the aim of the research is defined, and the research questions are stated.
- **Chapter 2** presents a more in-depth methodology applied to answer the research question. It begins with an overview of a case study and an experimental study. Subsequently, the wave-structure interaction relevant to this study is described. The chapter then presents the numerical model framework, definition of boundary conditions, and addresses the approach to answer the first research sub-question. In the final sections of this chapter, the numerical domain and setup are defined. Further, this chapter demonstrates the capabilities of OpenFOAM by comparing 2DV model results to an experi-

mental study by Goda. This case study was conducted to perform preliminary validation associated with normally incident waves interacting with a straight wall in order to provide a foundational understanding of the wave-wall interaction.

- **Chapter 3** presents an analysis of the 2DV model of the case study, followed by validation of the three-dimensional model of the case study. In the final section, the results of the spatial and temporal force distribution obtained from the three-dimensional model are provided.
- **Chapter 4** provides an in-depth discussion of the results presented in Chapter 3, highlighting the capabilities of OpenFOAM and pointing out limitations of the numerical model. Furthermore, this chapter describes practical implementations of CFD modeling for the design of structures.
- **Chapter 5** presents the conclusions drawn from this study and provides recommendations for future research.

2

Methodology

This chapter explains the methodology used to achieve the results of this study. It includes an overview of the case study, outcomes of the literature study, and setup of the numerical models. These methodological steps, delineated as Steps 1 through 3, are described in Section 1.3.

2.1. St. Petersburg flood protection barrier

St. Petersburg is a city in Russia that is located in a low area and is located in the eastern part of Neva Bay. In the past, the city has experienced severe floods due to the storm surges that can travel from the Baltic Sea. The city was founded in 1703, and since then, floods have been recorded almost annually, occurring whenever the water level exceeded +1.6 m above mean sea level. Moreover, between 1980 and 2002, the flood frequency increased (Hunter, 2012). The most severe flood happened in 1824, when the water level rose to +4.25 m Still Water Level (SWL).

The flood history of St. Petersburg city led to a project that involved the construction of a 25 km long flood protection barrier between Neva Bay and the Gulf of Finland, see figure 2.1.

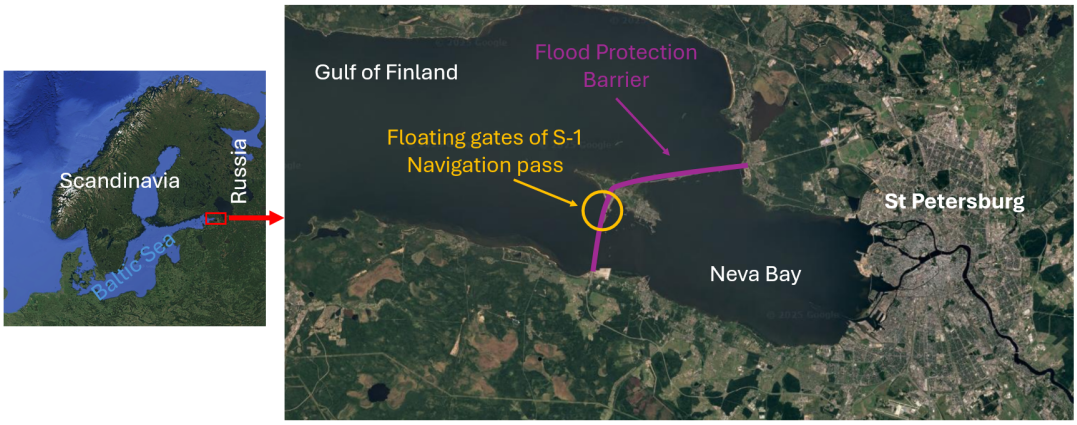

Figure 2.1: Location of St. Petersburg Flood Protection Barrier

The flood protection barrier has different elements, such as embankment dams and sluice complexes, but also a navigation channel with a storm surge barrier and movable sector gates. These floating gates for the S-1 navigation pass were designed in the 1980s-1990s. However, due to the postponed project, the gate was completed in 2011; the gate can be seen in Figure 2.2. The gates span a width of 200 m, with the crest elevation positioned at +7.5 m relative to mean sea level. Each gate leaf has a curved geometry with an approximate radius of 130 m.

Figure 2.2: The S-1 navigation pass, St Petersburg Flood Protection Barrier (Kozin, 2024)

Prior to construction, the designed gates underwent a series of 2DV and 3D physical model experiments. One of the 3D experiments in 2009 was conducted in St. Petersburg in order to investigate the wave load on the gates. The model was set up at 1:60 scale, consisting of a hung-up rigid frame in the position of the closed gate. The setup was arranged in such a manner that the frame did not make contact with the bottom.

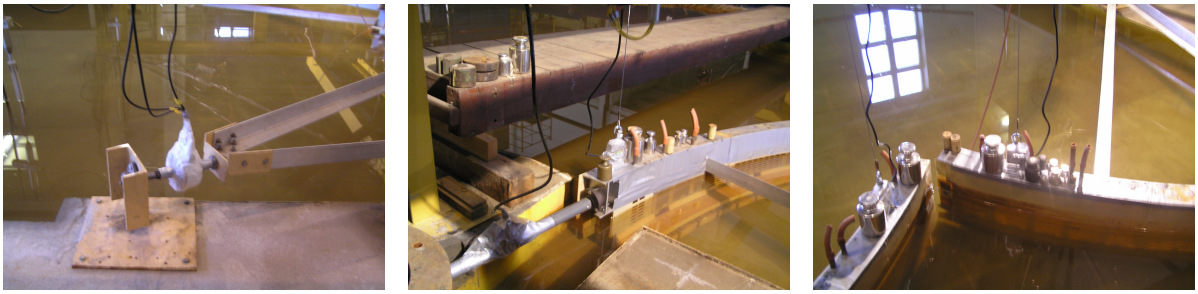

(a) Force sensor on supporting hinge **(b)** Force sensor on the tractor bar **(c)** Force sensors on the stern and bow

Figure 2.3: Overview of the sensors in the experimental set-up

The experiments have been conducted for wave incidence of $0°$, $10°$, and $20°$ for three hydraulic conditions. As the scope of this study excludes the effect of oblique incidence, the numerical analysis is restricted to investigating the effects of waves approaching normal to the gap between the breakwaters, as illustrated in Figure 2.4.

The experimental studies for all cases were tested with regular wave conditions. The wave height H that was used in the experimental studies corresponds to the $H_1\%$, based on the wave spectrum for the design condition.

The three hydraulic conditions tested in the laboratory correspond to representative in-field conditions near the barrier, as summarized in Table 2.1. However, due to computational resource limitations associated with the 3D model simulations, it was only feasible to analyze a single hydraulic scenario. Consequently, the Main Case (hydraulic condition 1) was selected for detailed numerical analysis.

In the physical experiment, the hydrostatic pressure was recorded before the operation of the wave maker. To maintain consistency, the numerical model employed a similar approach, whereby the dynamic pressure was obtained by subtracting the initial hydrostatic pressure (at t = 0 s) from the total pressure values.

In the physical model experiments, only the first 10-12 representative generated waves were taken into analysis for cases 1 and 2. For case 3, the first 3-5 generated waves were taken into analysis. This was done to minimize the influence of reflected waves from the walls of the flume and the structure, because after a certain time interval, the reflected waves were propagating back to the wave maker.

Number	Case	Gulf of Finland water level [m]	Neva Bay water level [m]	H [m]	T [s]
1	Main case	4.55	1	4.03	5.9
2	Checking case	5.15	1	4.15	5.9
3	Special case	4.55	1	2.9	9.3

Table 2.1: Hydraulic conditions of the case study

The forces were measured for both Southern and Northern gates. Every gate in the experimental setup had a three-axis force sensor on the supporting hinge, the tractor bar, and a vertical sensor in the stern and bow. These sensors can be seen in Figure 2.3. The forces were measured in three directions. The 0-coordinate is placed at the center of the hinge. The z-direction is the vertical direction, the x-direction is in the horizontal plane along caissons towards the center between two gates, and the y-direction is in a horizontal plane through the center of the gate towards the gates, as can be seen in Figure 2.4.

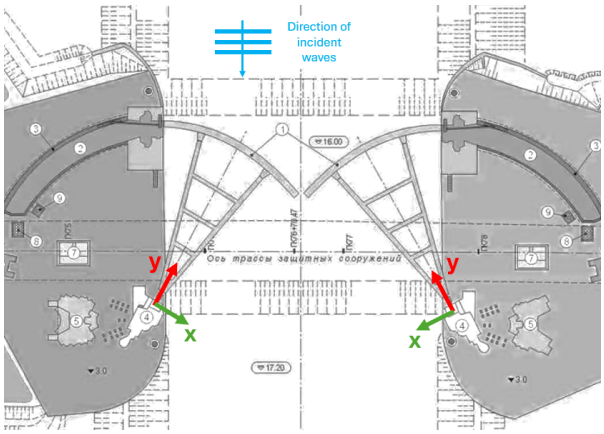

Figure 2.4: Coordinate system for measured in the experiment forces

In the physical model experiments, the main focus was on the extreme dynamic wave loadings. These extreme wave loadings that were measured in the physical model experiments are summarized in the table 2.2.

	F_x [MN]	F_y [MN]	F_z [MN]
Southern gate	-7.0	-17.0	-1.8
	3.1	16.2	1.5
Northern gate	-1.7	-12.2	-1.4
	4.5	9.5	1.2

Table 2.2: Overview of experimental dynamic extreme wave loading measured by the sensor on the supporting hinge under normal wave incidence at the domain entrance

As a result, in the numerical study, the case study is simplified to a single gate model, under the assumption that both gates are symmetric and are placed in a closed position. The computational model is set up at full prototype scale, corresponding to real-life dimensions. Regular, normally-incident to the boundary of domain wave conditions, corresponding to Case 1 as

specified in 2.1, are applied for validation of both the 2DV and 3D numerical models, as well as for the evaluation of the resulting force distribution on the structure. In contrast to the experimental study, where the force measurements were conducted at the hinge mechanism, the numerical model determines the dynamic forces by integrating pressure data obtained from numerical pressure sensors distributed over the surface of the gate structure.

2.2. Mesh sensitivity analysis

A mesh sensitivity analysis was conducted by testing computational grids with resolutions of 8, 12, 16, and 32 cells per wave height. Figure 2.5 presents a visual representation illustrating the computational grid configuration per wave height for each tested resolution.

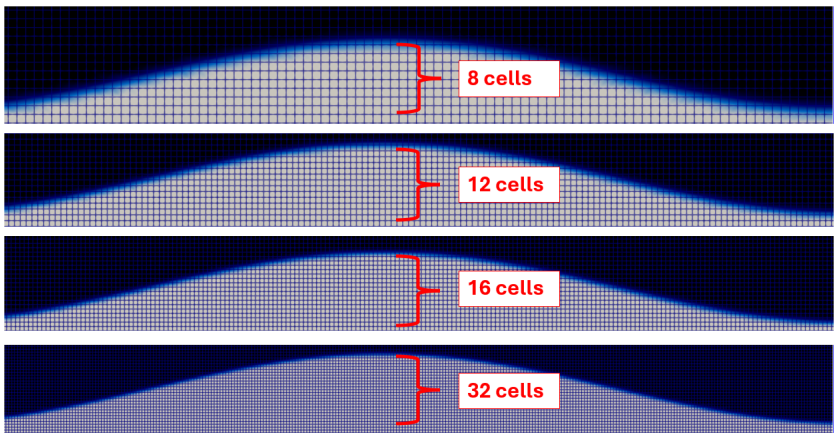

Figure 2.5: Visual representation of the number of cells per wave height

The surface elevation time series recorded by the wave gauge in the numerical model, adjacent to the wall of the 2DV St. Petersburg setup, indicate that 16 cells per wave height is very close to the case with 32 cells per wave height, as illustrated in 2.6 However, during the development of 3D model, it became evident that the available computational resources were insufficient to create a mesh with 16 cells per wave height. As a result, a mesh with 12 cells per wave height was chosen for the 3D case because it provides a suitable balance between accuracy and computational efficiency. The degree of precision provided by this mesh is illustrated in Figure 2.6, where the wave time series in a model with 12 cells per wave height closely align in both shape and magnitude with results of both 32 and 16 cells per wave height, while showing a better agreement than the waves in a model that was set up with 8 cells per wave height.

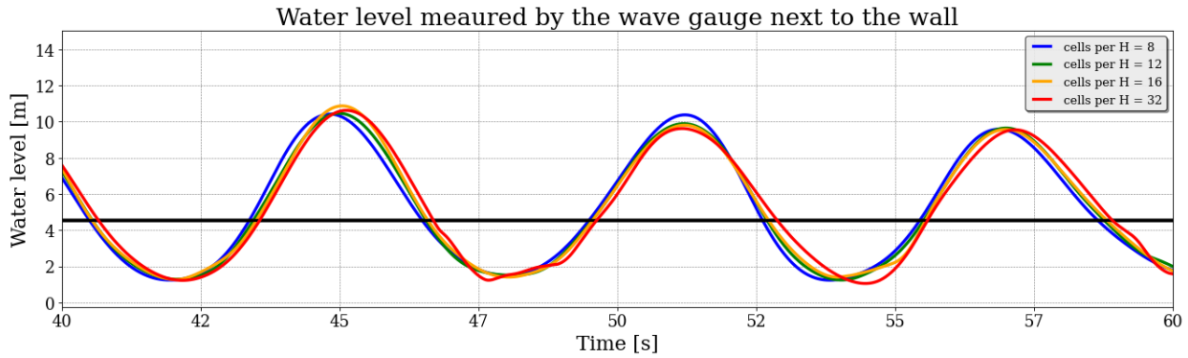

Figure 2.6: Timeseries of the water level elevation for the wave gauge next to the wall of the 2DV St. Petersburg model

2.3. Wave-structure interaction

One of the most important factors in evaluating forces acting on a structure is the reflection. In a two-dimensional case with a rigid wall, according to theory, a standing wave pattern emerges. Theoretically, the incident wave is fully reflected and travels in the opposite direction of the incoming waves. However, it should be noted that in practice, the reflection is not fully reflected, and a portion of energy is dissipated through interaction with the structure and other physical processes.

The superposition of the incident and reflected waves leads to a standing wave pattern with the first node occurring at one-quarter of the incoming wavelength distance from the vertical rigid structure; see Figure 2.7. As illustrated in Figure 2.7, the horizontal particle velocity component reaches its maximum at the nodes, whereas the vertical particle velocity component reaches its maximum at the antinodes. Due to the superposition of incoming and reflected waves, the total wave height is twice the size of the incoming wave height.

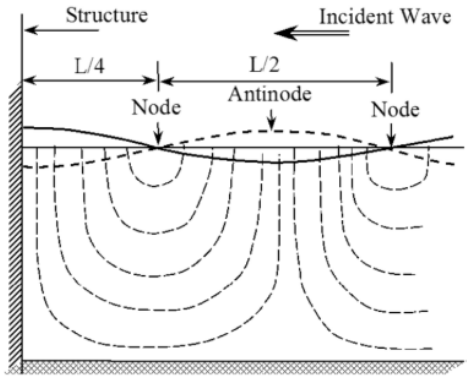

Figure 2.7: Standing waves. Dashed lines represent stream lines(Kamphuis, 2020)

Dynamic pressure on a wall

According to Goda (1967), standing waves in the deep water result in two pressure fluctuations beneath the water surface during one wave period. These fluctuations result in the double humps that can be seen in the pressure time series, characterized by different harmonic components (Goda, 1967). An example of such double humps in the pressure on a vertical wall timeseries is shown in Figure 2.8. Based on the theoretical framework of Goda (1997), it can be expected that in a 2DV case with regular waves, this characteristic double hump pattern will appear in both the measured pressure and corresponding force time series.

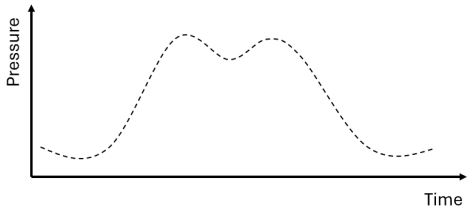

Figure 2.8: Example of integrated pressure on a vertical wall timeseries

In order to estimate and predict the type of wave load that can be seen in the time series, the PROVERBS (Probabilistic Design Tools for Vertical Breakwaters) parameter map can be addressed; see Figure 2.9. This map gives the possibility to estimate the expected load type based on the geometrical and wave characteristics. Therefore, the most important indications for the load type are the geometry of the structure and hydraulic conditions.

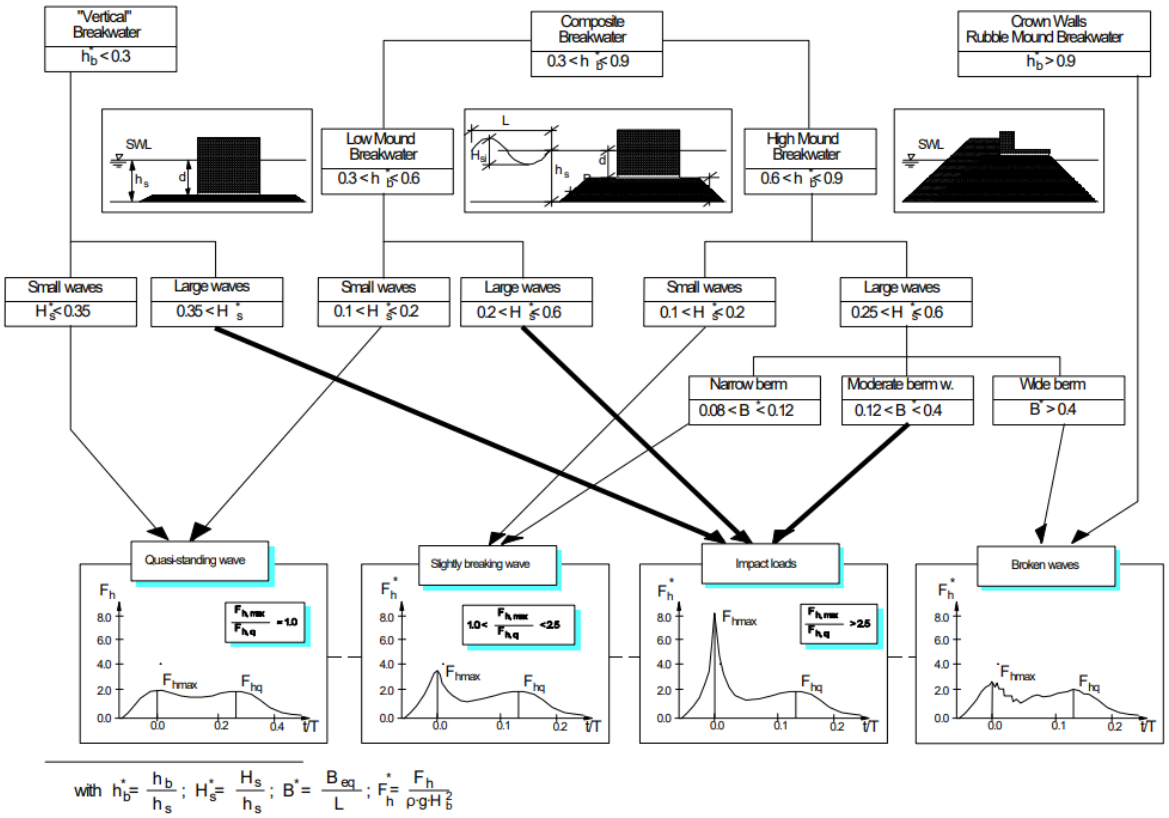

Figure 2.9: PROVERBS parameter map (Kortenhaus et al., 2001)

The vertical wall is similar to the vertical breakwater, which according to the Figure 2.9 can lead either to Quasi-standing or Impact loads. The quasi-static (or quasi-standing) leads to the double humps in the forcing time series that are similar to one another, and the impact load has one peak (the impact peak) that is significantly larger than the second peak, as can be observed in Fugure 2.9.

In the case study from Section 2.1, the wave height is a minimum of 2.9 m and a maximum of 4.15 m. This corresponds to H_s^* of 0.14 and 0.20, respectively. According to the Figure 2.9, these conditions represent the small waves and quasi-standing wave load on the structure. Consequently, the expected force time series is expected to display two peaks due to the

incoming wave and reflection. Based on this theoretical approach, it can be assumed that there are two main load cases present: hydrostatic and quasi-static loads when looking at a 2DV case.

The hydrostatic load is present when pressure is induced on the structure by the mean water level and considered to be constant under the assumption of no temporal variation of the mean water level and calculated with equation 2.1. In this study, only the dynamic load is considered by subtracting the hydrostatic load of the mean water level from the measured pressures.

$$p_s = \rho g d \tag{2.1}$$

The quasi-static load is the load that does not have inertial effects and is present only when waves are present. According to Kortenhaus et al. (2001), the most important empirical methods for calculating the magnitude of the pressure on a vertical wall due to quasi-static wave load are Saintflou (1928), Miche-Rundgren (1944, 1958), and the most widely-used Goda (1974). In this research, the 2DV results will be compared to Saintflou (1928), Goda (1985), and Linear Wave Theory.

Linear Wave Theory (LWT)

The linear wave theory, as described in equation 2.2, is applicable in the determination of wave pressures induced by non-breaking waves on a wall. According to this equation, the quasi-static wave pressure varies in phase with the surface elevation. In quasi-static conditions, the actual pressure is a sum of hydrostatic pressure and quasi-static pressure with the maximum under the wave crest and minimum under the wave trough, see the Figure 2.10.

$$p_d = \rho g A \frac{cosh(k(h+z))}{cosh(kh)} \tag{2.2}$$

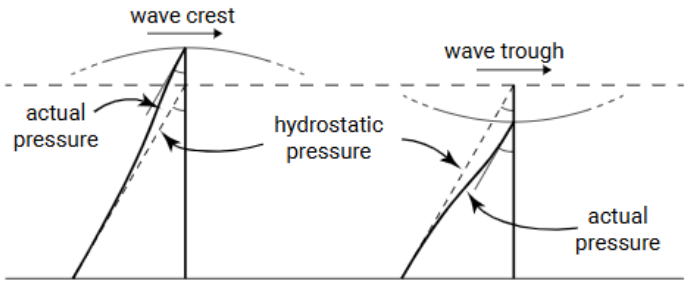

Figure 2.10: Wave-induced pressure oscillations in deep water

Sainflou

The Sainflou (1928) empirical wave pressure formula is based on Stoke's second-order wave theory. It can be primarily used for standing waves as it can be applied to steeper waves compared with the LWT (van Vledder et al., 2019). This method works under assumptions of non-breaking, standing waves, and a full reflection of the waves from the wall. The increase in the SWL (Still Water Level) is taken into account in equation 2.3, the maximum pressure at the water surface is calculated with equation 2.4 and the pressure near the bed is calculated with equation 2.5.

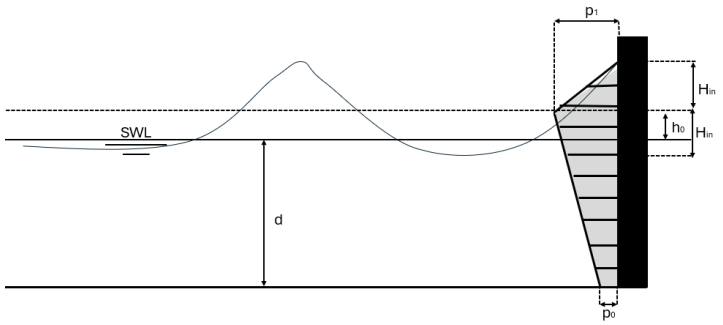

Figure 2.11: Wave-induced pressure distribution according to Sainflou (1928)

$$h_0 = 0.5kH_{in}^2 \cdot coth(kd) \tag{2.3}$$

$$p_1 = \rho g(H_{in} + h_0) \tag{2.4}$$

$$p_0 = \frac{\rho g H_{in}}{cosh(kd)} \tag{2.5}$$

Goda (1974)

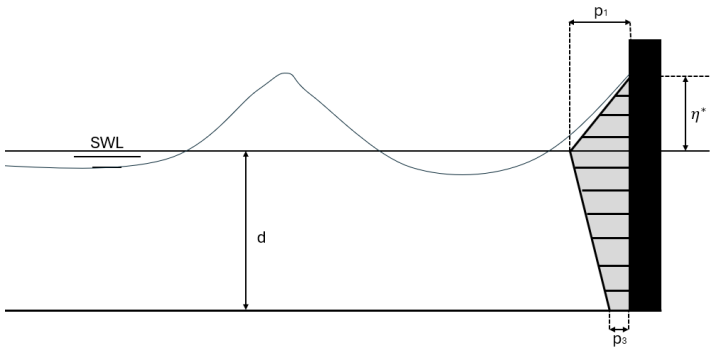

Figure 2.12: Wave-induced pressure distribution according to Goda (1974)

The empirical expression for the wave pressure distribution on a vertical breakwater was derived by Goda in 1974, based on a series of physical model experiments. The original expression is applicable for breaking and non-breaking waves.

The original formula of Goda takes into account the geometry of the breakwater. Since, for the purpose of this study, the straight wall with normal incident waves is considered, the factors that account for the complexity of the structure can be neglected, and the pressures based on the Goda (1974) formula can be calculated as presented in equations 2.6, 2.7,2.8.

$$p_1 = (0.6 + 0.5(\frac{2dk}{sinh(2dk)})^2 + \frac{2d}{H_D})\rho g H_D \tag{2.6}$$

$$p_0 = \frac{p_1}{cosh(kd)} \tag{2.7}$$

$$\eta^* = 2 \cdot 0.75 H_D \tag{2.8}$$

2.4. Force application point calculation

In order to calculate the application point of the resulting force on the structure along the gate, the moment sum of forces measured is divided by the sum of all individually measured forces.

The formula used to calculate the application point along the curvature of the gate expressed by coordinate *s* on the XZ-axis is given in Equation 2.9.

$$s_{\text{total}} = \frac{\sum_{i=1}^{n} F_i \, s_i}{\sum_{i=1}^{n} F_i} \tag{2.9}$$

The formula used to calculate the application point along the *y* coordinate (height of the gate) is given in Equation 2.10.

$$y_{\text{total}} = \frac{\sum_{i=1}^{n} F_i \, y_i}{\sum_{i=1}^{n} F_i} \tag{2.10}$$

2.5. Numerical model description

OpenFOAM

OpenFOAM (Open Field Operation and Manipulation) is an open-source CFD model that uses the C++ library for solving Reynolds averaged Navier-Stokes equations coupled with the volume of fluid method (VOF) (Weller et al., 1998). Over the years, this model has had different applications, which have enhanced its capability to be applied to complex coastal processes. In 2012, the waves2foam toolbox was developed, which extended OpenFOAM with the addition of a relaxation zone, reflection, and absorption of waves, which was demonstrated with propagating and breaking waves (Jacobsen et al., 2012).

One of the CFD models is the CoastalFOAM package developed by the Joint Interdisciplinary Project (JIP), framework of which can be seen in Figure 2.13. The JIP was established in 2015, which included Deltares, Van Oord, Boskalis, and Royal HaskoningDHV. JIP has created the extended version of OpenFOAM, which is referred to as CoastalFOAM. The CoastalFOAM package integrates the OpenFOAM framework with the waves2foam toolbox. Additionally, it is capable of implementing a ventilated boundary layer application, which can resolve air entrapment due to the impact of breaking waves. The CoastalFOAM package enables numerical investigation of a wave-structure interaction, using Navier-Stokes.

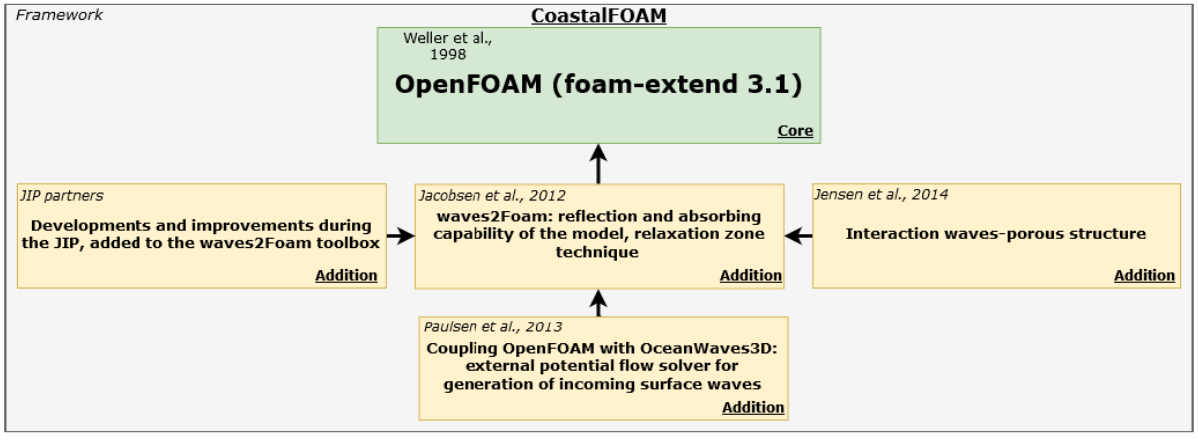

Figure 2.13: OpenFOAM model with waves2foam, waves-porous structures and coupling with OceanWaves3D additions Moretto, 2020

Finite Volume Method (FVM)

Finite Volume Method is a discretization technique of the partial differential equations (PDEs), and it is commonly used in computational problems related to flow. It uses a volume integral formulation (Chenlong, 2025). The domain is divided into cells (control volumes), and then the governing PDE is integrated over each cell. The equation that is being solved is Reynolds' averaged Navier-Stokes equation.

In general, there are two types of FVMs: cell-centered and vertex-centered. In this study, the cell-centered scheme is employed, as it is the discretization scheme that is used in OpenFOAM. In the cell-centered approach, FVM discretization is carried out in such a way that information on incoming and outgoing fluxes through mesh cell faces is stored in the center of a cell.

Volume of fluid (VOF)

The volume of fluid is the method that allows for tracking and capturing the water and air interaction. The VOF achieves this by describing the fraction of air and water for each cell, which is obtained from equation 2.11 (Gamet et al., 2020). This phase fraction is α, and when it equals 1, it is pure water. When α is 0, it represents pure air. Therefore, all values between 0 and 1 represent an interaction between air and water.

$$\frac{\partial \alpha}{\partial t} + \nabla \cdot (\alpha \mathbf{u}) = 0 \tag{2.11}$$

2.6. Boundary conditions

The numerical domain is defined by patches at its boundaries to which different boundary conditions can be applied. The overview of the names of the patches can be seen in Figure 2.14. These patches have the following boundary conditions that are assigned to variables, such as pressure (p), phase fraction (α), and velocity (U):

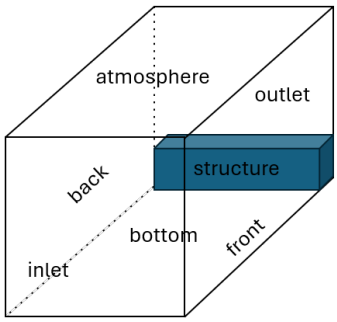

Figure 2.14: Overview of numerical patches of the domains used in this study

Inlet

This patch is at the side of the numerical tank where the waves are generated. Both 2DV and 3D cases have the *zeroGradient*, which means that the normal derivative of the variable (p, α or U) is 0 at that patch.

Outlet

This patch is at the end of the numerical tank, similarly to the *Inlet*, it has the *zeroGradient* boundary condition in 2DV and 3D cases.

Atmosphere
For both 2DV and 3D cases the boundary condition for α is *inletOutlet*, for U it is *pressureInletOutletVelocity* and for U it is *totalPressure*, which ensures a fixed pressure value.

Bottom
Bottom is the lower patch, representing the seabed. For both 2DV and 3D, the α and p boundary condition is *zeroGradient*. For U, the boundary is set to be *slip*. This corresponds to a normal velocity of the fluid at the boundary equal to 0, and there is no friction at this boundary.

Structure
Next to the outlet patch, the structure is represented by removing a volume of it from the mesh. At the boundary of the removed volume, the patch is applied to that phase. For both 2DV and 3D, the α and p boundary conditions are *zeroGradient*, and for U, the boundary is set to be *slip*.

Front
This patch is on one of the sides of the flume, as illustrated in Figure 2.14. For the 2DV case, it has *Empty* boundary conditions that allow for reducing the geometry to 2DV, and therefore, the variables are not solved in the third direction. In the 3D case, the boundary condition that is applied to p and α is *zeroGradient*. The boundary condition that is applied to U is *slip*.

Back
For 2DV case this patch has the *Empty* boundary condition, similarly to Front patch. However, for the 3D case, only half of the gate is modeled, and the gates are assumed to be symmetrical. Therefore, the *symmetryPlane* boundary condition can be applied to p, α and U as well as the patch type is defined as *symmetryPlane*. *symmetryPlane* is a boundary condition where the solution is mirrored across the boundary where it is applied. This boundary condition is suitable for domains with symmetric flows and geometry (Greenshields, 2024). By applying this boundary on the plane where 2 gates converge, a model can simulate the behaviour of the system with two gates while modeling a single gate. This boundary enhances efficiency when dealing with symmetrical domains.

2.7. Grid Resolution
Generally, meshes can be classified into two categories: structured and unstructured. Structured meshes are characterized by a repetitive pattern. In contrast, unstructured meshes exhibit an irregular pattern and, unlike structured meshes, do not fit the Cartesian coordinates (in 3D, those are i, j, k). This irregularity results in additional computational processes to solve flow between the cells, resulting in larger computation time and lower efficiency in comparison to structured meshes (Lintermann, 2021).

The primary advantage of the unstructured meshes lies in flexibility for solutions of flow within complex geometries. In regions where a geometry interacts with the flow, an unstructured mesh allows for accurate capture of the complex shape of the geometry with its irregularity. One of the approaches to do so is the use of *SnappyHexMesh* for adding the irregular cells around a geometry to the structured mesh in order to follow the shape of the structure. An example of such implementation is illustrated in Figure 2.15. Therefore, in the set-up of the model in this study, the structured mesh was used, and the irregular cells around the complex structure, in combination with the regular cells, were generated using *SnappyHexMesh*.

A mesh consists of smaller elements, called cells, that can have a specific shape, in the case of a structured mesh. For the 2DV model, the quadrilateral cells were used. For the 3D case, the

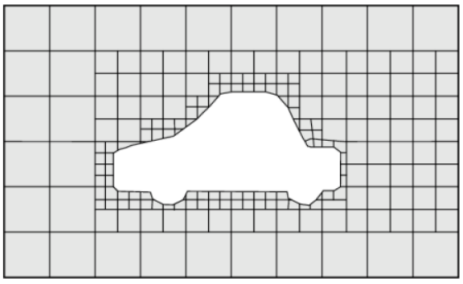

Figure 2.15: Surface snapping around a complex shape with *SnappyHexMesh* (Greenshields, 2024)

hexahedron, presented in Figure 2.16, was used. This shape is one of the most common cell types. The use of a hexahedron as a mesh cell type is due to the mesh quality considerations.

After *SnapyHexMesh* was used, around the structure, the cell types, such as prisms and polyhedral cells, were used in order to capture the shape of the sector gate geometry.

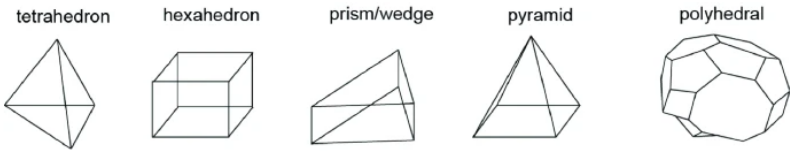

Figure 2.16: Possible 3D mesh elements (Lintermann, 2021)

The quality of the created mesh is influenced by the cell shape that can be measured in skewness, orthogonality, and aspect ratio. Skewness is determined by the angle between the grid lines of the mesh. For Cartesian meshes, the most optimal and efficient angle is $90°$ (Lintermann, 2021). The orthogonality is the alignment of the cell faces that have to be perpendicular to the flow or the vector. This implies that if the cells are not aligned with the flow, meaning that cells are not orthogonal, the information from the cell center to the cell center is passed through an angle, which may result in significant numerical diffusion.

The aspect ratio is the proportion of the horizontal size of the cell to the vertical size of the cell. An example of the aspect ratios can be seen in Figure 2.17. The aspect ratio for the cell should be between 0.2 and 5 (Lintermann, 2021). Therefore, for the set-up of the basic mesh, the aspect ratio 1 was used, meaning that in the 2DV case, $dx = dy$, and in the 3D case, $dx = dy = dz$.

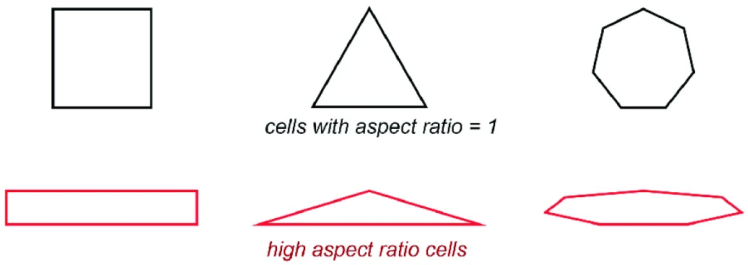

Figure 2.17: Aspect ratio of a mesh cell (Lintermann, 2021)

Previous research shows that in 2DV CFD simulations with regular waves, the larger the mesh cell sizes are, the more wave energy dissipation occurs. This typically leads to lower accuracy of the results, which is evident from the lower surface elevation (Marques Machado et al.,

2018). This implies that an increase in the cell size in a given direction would lead to an increase in numerical dissipation in that direction.

Consequently, for setting up a numerical model, the number of cells per wave height and the wave length are of great importance for resolving the water surface elevation correctly with the VOF. The guideline of JIP CoastalFOAM for the mesh resolution in horizontal (x-direction) suggests using a minimum of 100-150 cells per wavelength and a minimum of 5-10 cells for wave height in the vertical direction (y-direction). Prior to running the final model, the cell size sensitivity analysis has to be conducted. In this research, the sensitivity analysis was done to check 8 cells, 12 cells, 16 cells, and 32 cells per wave height.

2.8. Domain definition

The bathymetry of the area has many aspects. As can be seen in Figure 2.18, in the width, the area around the sector gates has complex bathymetry aspects, as for example, breakwaters. Moreover, the area is relatively asymmetrical as a whole. In this study, the spatial variations in the width of the area are outside of the scope, and the domain is assumed to be symmetric.

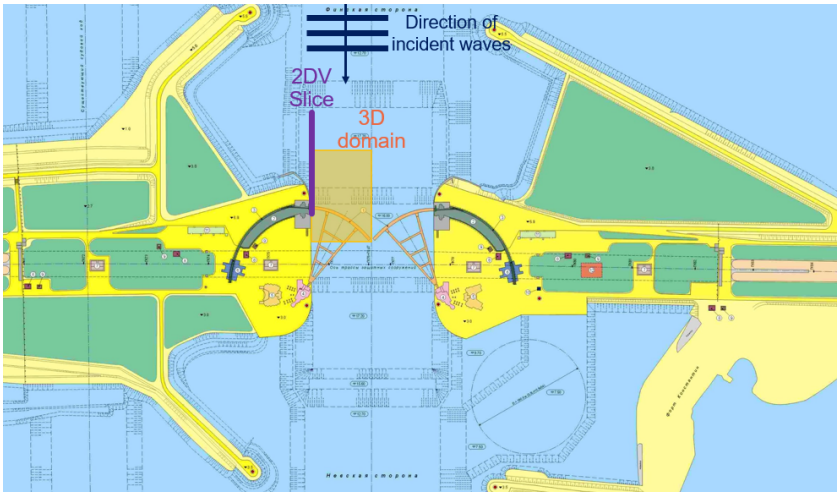

Figure 2.18: Top view of the area around the S1 passage with defined modeled wave incidence direction and numerically analyzed in 2DV and 3D models

In the length of the area of the case study, there are variations in depth. At the Gulf of Finland side, immediately outside of the breakwaters, the seabed is positioned at -12.7 m. Progressing towards the gate, depth increases, and the seabed is positioned at -17.2 m. Directly beside the gate, there is a 45 m long sill that reduces the depth to -16.0 m. In order to evaluate this cross-shore variation in bed levels, the OpenFOAM and OceanWave3D (OCW3D) models were set up. The OCW3D is a fully non-linear and dispersive potential flow model. The assumptions that hold in this model are that waves are non-breaking and fluid flow is inviscid, irrotational, and incompressible. This model has shown agreement with theory and experimental studies for steep nonlinear waves and shoaling problems and is suitable for simulating wave-wave, wave-bottom, and wave-structure interaction (Engsig-Karup et al., 2009). The OCW3D run was conducted to check its accordance with the OpenFOAM-based model.

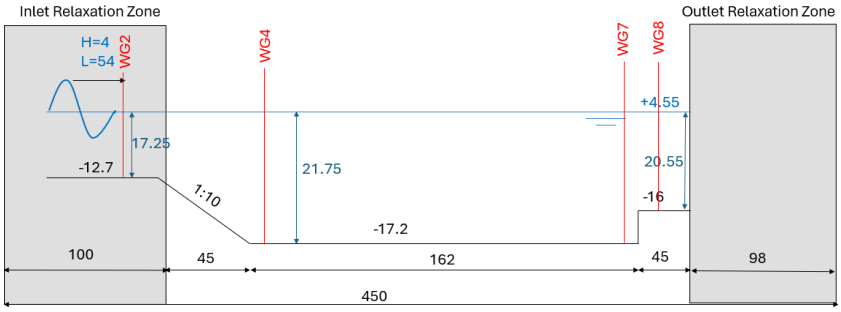

Figure 2.19: Set-up for evaluation of bathymetry on the wave propagation along the flume

The setup for both models is identical: there is a flume place with variations of bathymetry (that can be seen in Figure 2.19), and the wave gauges have been placed every 50 m. The OpenFOAM setup used a mesh that corresponds to 16 cells per wave height around the water surface, and the OceanWave3D has 10 layers, which, according to (Mata, 2021), is sufficient. The run was conducted for 400 s, and only the last 100 s have been analyzed.

The results presented in Appendix A show that the wave propagation in the OceanWave3D closely matches the wave propagation of OpenFOAM at the inlet of the flume; however, noticeable differences in the results of the models appear closer to the outlet. For both models, it applies that the water elevation of the runs with bathymetry variations (in comparison to the runs for both models without the bathymetry variations) is not significant on the scale of the wave height in the flume. After the water deepens, around 100-150 m, the maximum water level measurement from Figure 2.20 suggests a slight wave height decrease, which corresponds with theory. When the wave propagates to deeper water, wave speed increases, so does wave length, and the wave height decreases. When the water level decreases at the sill next to the gate, the wave speed decreases; hence, the wave length shortens and the wave height slightly increases, as can be observed in Figure 2.20.

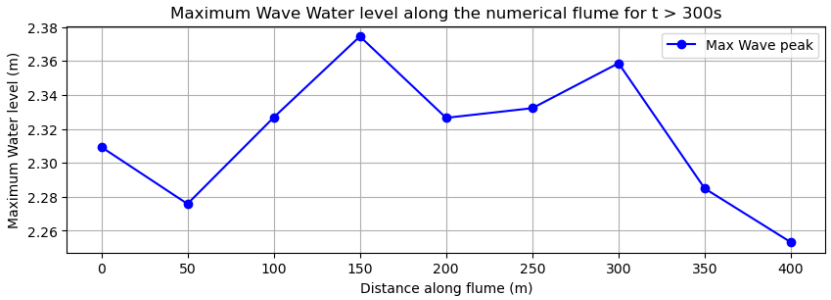

Figure 2.20: OpenFOAM run with bathymetry variation, maximum water elevation per gauge for t>300

Given the computational intensity associated with modeling a 400 m domain in OpenFOAM, particularly when extended to 3D, and considering the minimal influence of wave height variations observed in the preceding analysis, it can be concluded that the numerical flume bathymetry of the 2DV and 3D setups will not include bathymetry variations.

As a result, the length for the 2DV case was set to three and a half wavelengths (195 m), following the recommendations of the JIP guidelines. For the 3D case, this length was reduced to two wavelengths (110 m), and only the domain corresponding to a single gate was modeled. Consequently, the width of the 3D numerical flume was defined as 100 m, corresponding to

the width of one gate. The modeled sections of the computational domain for both cases are illustrated in Figure 2.18.

2.9. Numerical set-up

The validation of the model is carried out in several steps. Before validating the 3D model, the pressure distribution is first validated in a 2DV model. To achieve this, a similar experimental study in 2DV was reproduced with the CFD model. In the second step, the St. Petersburg case was reproduced in 2DV numerical model and compared against empirical relations and Linear Wave Theory. The final step involves extending the 2DV model to a 3D model and comparing the forces obtained from the 3D simulations to the corresponding experimental data. An overview of these validation steps is shown in Figure 2.21.

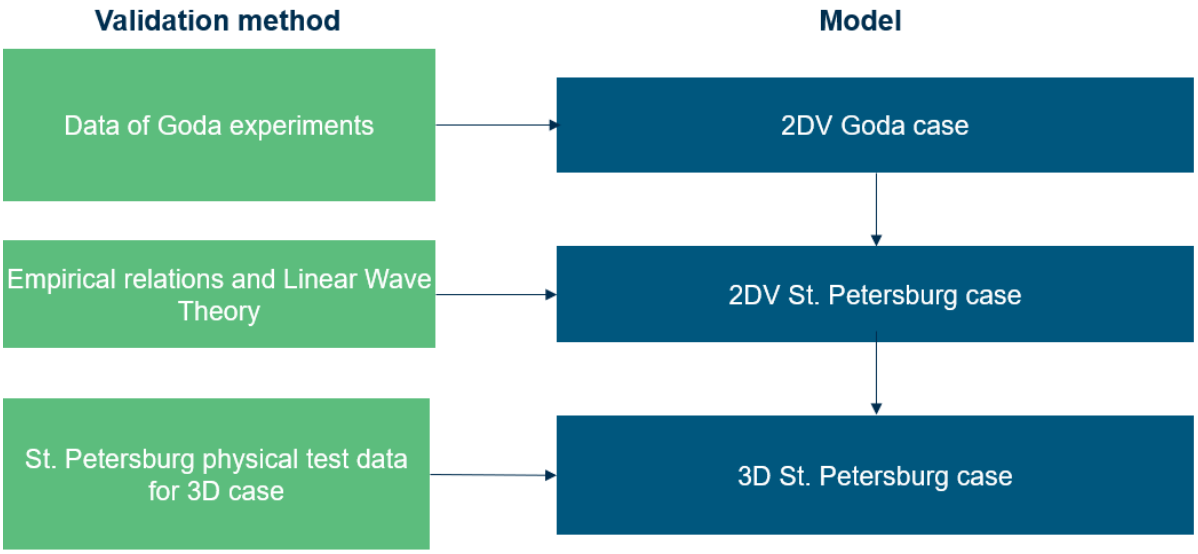

Figure 2.21: Overview of three models that were set up and the validation methods that were applied to validate/compare the results

2.9.1. 2DV validation based on Goda 1966

The available data for the St. Petersburg case, as described in Section 2.1, does not include time series measurements, such as wave gauge measurements and/or pressure sensor measurements. In order to validate the 2DV model for the St. Petersburg case study, another case study has to be used that has similar hydraulic conditions.

In 1967 Goda has published research on the fourth-order approximation for the determination of the wave pressures on the breakwater. The fourth-order approximation has been compared to the results of the experiments that have been conducted in the lab in the 105 m channel with regular waves (Goda, 1967). The detailed results of the experiments and analysis were published in the original paper (Yoshmi Goda, 1966). Appendix B of Yoshmi Goda, 1966 paper presents results for the experiments with different d/L_A and H/L_A ratios.

The experimental study presented in the paper of Yoshmi Goda, 1966 with ratios of $d/L_A = 0.3$ and $H/L_A = 0.06$ are used as the validation case for the 2DV model. These ratios exhibit a good agreement with those determined for the St. Petersburg wave condition, which are $d/L_A = 0.4$ and $H/L_A = 0.07$.

The set-up for the numerical simulation based on the experiment that was conducted by Goda is presented in Figure 2.22. The numerical wave flume has a height of 0.8 m and a length of

7 m with an input relaxation zone of 2 m.

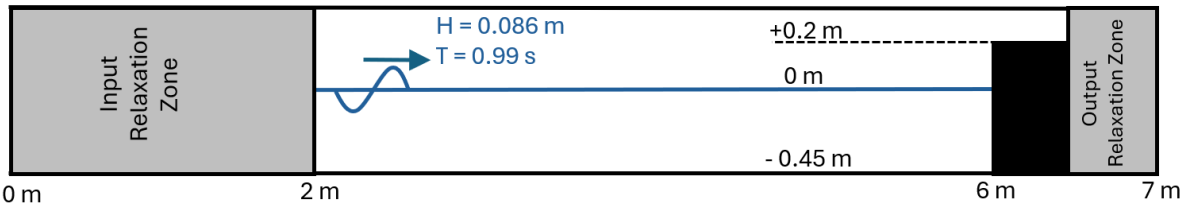

Figure 2.22: Overview of the numerical domain for the Yoshmi Goda, 1966

According to the suggestions of the Joint Industry Project (JIP), the basin length without the structure has to be approximately 4 m, and an inlet relaxation zone of 2 m. The grid cells before refinement around the water surface line were chosen to be squares with a side of 0.02 m. Therefore, after applying one level of refinement around the surface line, cells are the squares with sides of 0.01 m.

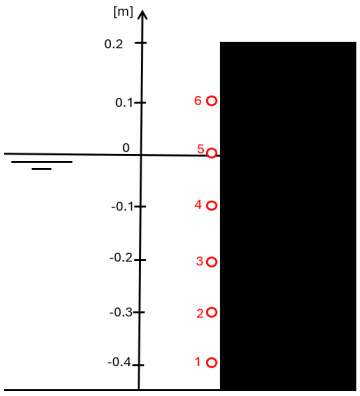

Figure 2.23: Set-up of 2DV model with pressure sensors marked by red numbered circles

In terms of numerical measurement devices, wave gauges were positioned in the numerical flume, including one located at the boundary with the wall. Furthermore, the pressure sensors were placed in the middle of the cells bordering the structure's face according to the measured pressures of (Yoshmi Goda, 1966). The set-up of the pressure sensors' positions can be observed in Figure 2.23.

For the pressure sensor data, the dynamic pressure was recorded for three situations: pressure when under the peak of a wave, through the wave, and the maximum recorded pressure, which can be seen in Figure 2.26 in grey.

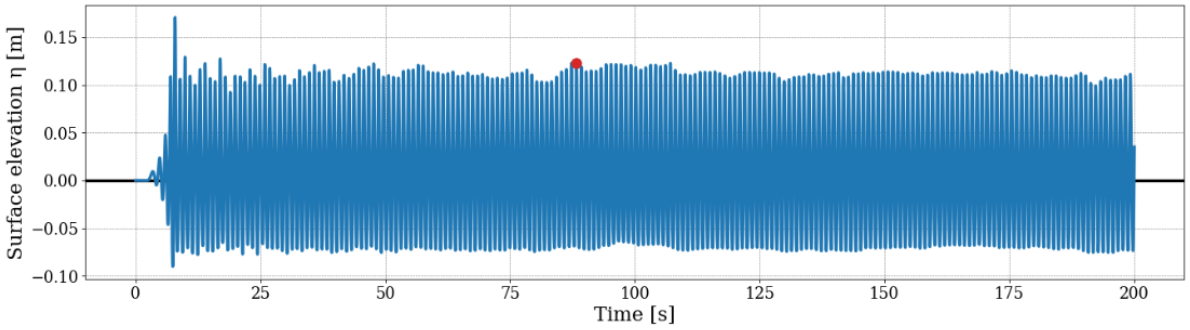

Figure 2.24: Raw data for the water level elevation with the maximum water level after 25 s

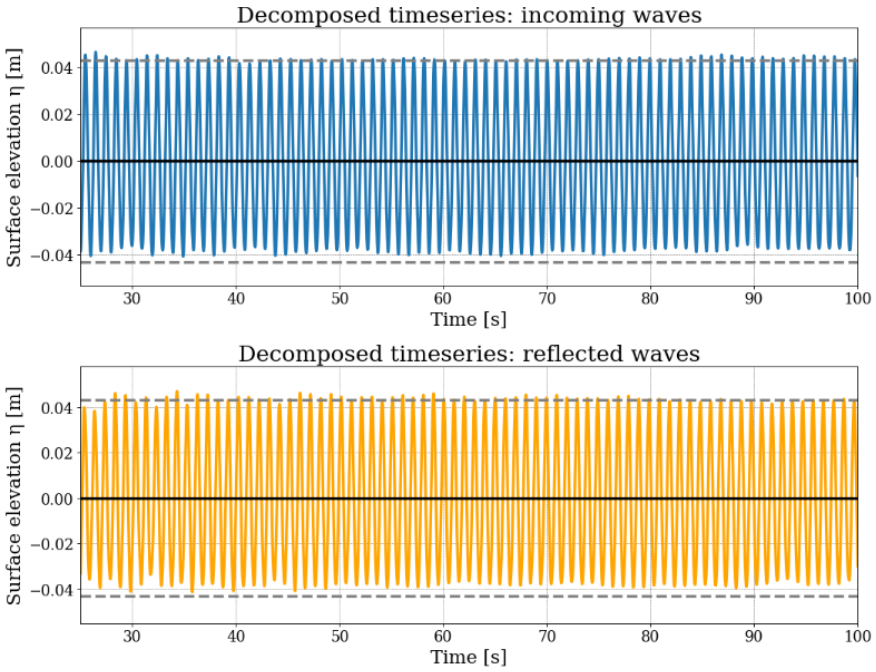

(a) Wave decomposition in incoming and reflected waves, with grey stippled line marking theoretical peak and trough of the waves

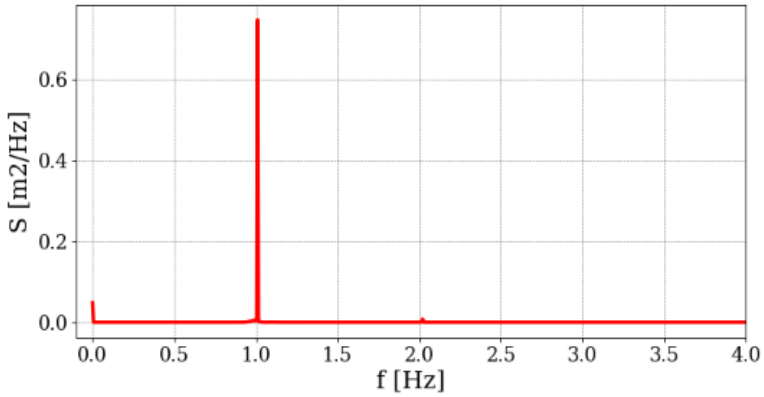

(b) The spectrum of 2DV CFD run based on experiments of Goda (1966)

Figure 2.25: Reflection analysis and spectrum analysis of numerical results of the case study of Yoshmi Goda, 1966 experiment

From the water surface elevation recorded in the numerical run, based on this study set-up, the highest wave in the series after 20-25 s of simulation was recorded.

Based on the water surface elevation recorded in the numerical simulation, the experimental set-up of Goda, the highest wave was identified for the time larger than 25 s. This is due to the fact that it takes the first 20-25 s for the numerical flume to reach a steady state, as is visually deducted by analyzing Figure 2.24. These time series were also decomposed into reflected and incident waves, which can be seen in Figure 2.25a. It is observed that both the incoming and reflected waves are above the theoretical wave trough (marked with a grey line). As shown in Figure 2.25b, there are two peaks present in the spectrum analysis, signifying the presence of second-order wave components in the domain. This explains the observed elevation of the wave troughs above the theoretical threshold in Figure 2.25a.

For further analysis, the wave marked by the red dot in Figure 2.24, which corresponds to

the highest measured wave height, is considered. For this wave, the time instant when the wave crest interacts with the structure was selected to capture the total pressure distribution. The dynamic pressure at each sensor was then obtained by subtracting the initial hydrostatic pressure from the total measured pressure.

The pressure values shown in in Figure 2.26 were extracted from the analysis of the highest wave (for crest and maximum pressure values) and from the largest trough (for trough pressure values) after the wave elevation time series had reached steady state (beyond 50 s). For the highest recorded wave crest at the wall structure, the dynamic pressure distribution for each pressure sensor was plotted as red dots in Figure 2.26. For the same wave, the maximum pressure instant was determined, which occurs prior to the wave crest, which is identified and illustrated in Figure 2.28.

The same procedure used to analyze pressures under the crest was applied to determine the pressure distribution over the water depth beneath the largest trough, which was identified at 52.2 s in the time series. The corresponding pressure distribution beneath this trough is also presented in Figure 2.26.

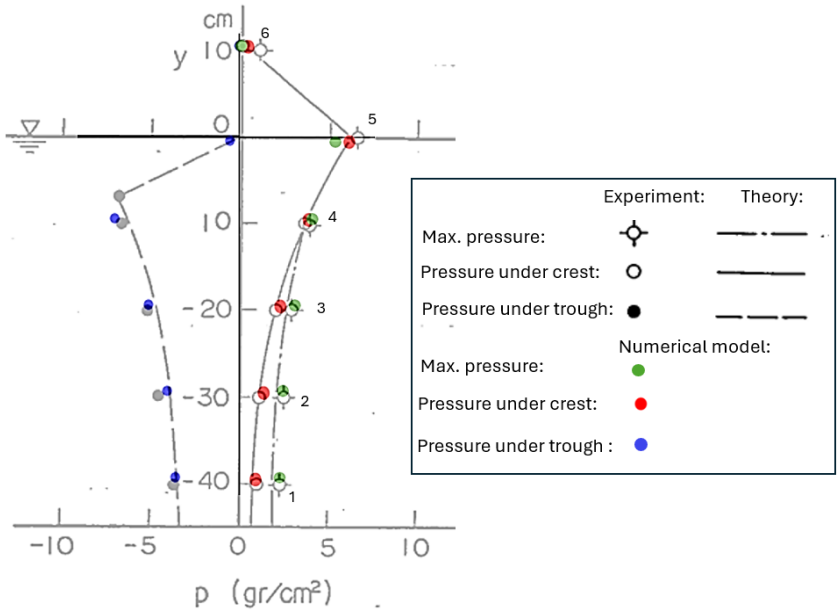

Figure 2.26: The comparison of results provided by Goda and the numerical simulation

From Figure 2.26, it can be observed that the dynamic pressures that were recorded in the numerical model are in good agreement with the pressure under crest data as well as the trough data that is presented in the research paper of Yoshmi Goda, 1966. Despite a coarse resolution of the data overlap, the overall dynamic pressure distribution pattern remains similar.

In Figure 2.27, the comparison of the dynamic pressures and water surface elevation at the interface with the wall is presented. For the highest recorded wave in the OpenFOAM model, the pressure time series are plotted and compared to the data recorded in the experimental study of Yoshmi Goda, 1966. It can be observed that the wave height of the largest wave recorded in the OpenFOAM model is greater than that measured in the experimental data. However, the dynamic pressure distribution obtained from the CFD model demonstrates a similar pattern to the experimental data. It should be noted that the comparison of the results was done by overlaying results through scaling, and the exact numerical values of Goda's experiments are not available. As a result, the accuracy of the comparison between experimental data and OpenFOAM 2DV model results is subject to certain limitations. However, the results presented by Yoshmi Goda, 1966 are compared to the numerical results in the figure 2.27. It can be observed that the temporal pattern of the pressure distribution is similar. Moreover, the magnitude of the numerical experiment is in the same order as the magnitude of the experimental studies. Therefore, it can be stated that the numerical 2DV model is in good agreement with the physical results.

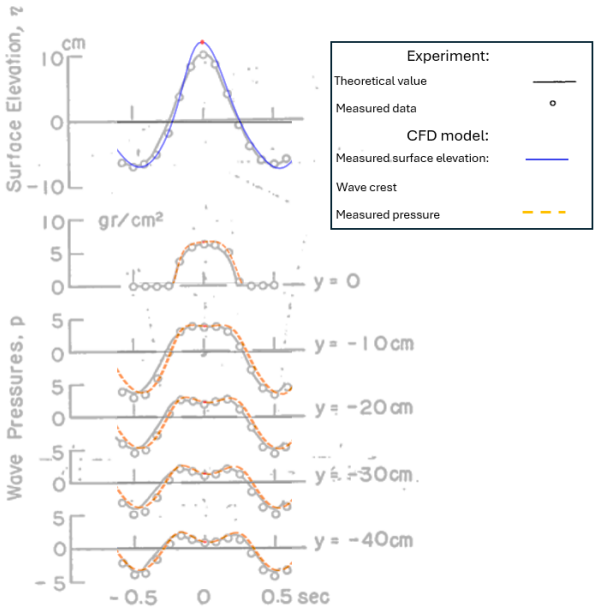

Figure 2.27: The comparison of pressures in time provided by Goda and the numerical simulation for pressure sensors 1 to 5

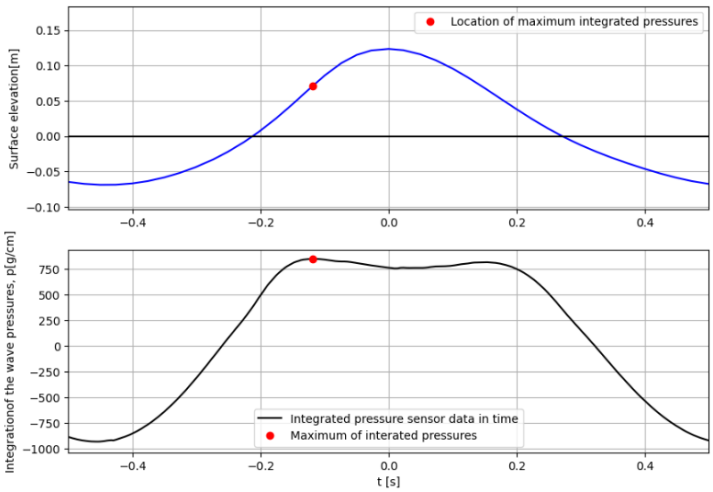

Figure 2.28: Integration of dynamic pressure measurements in time, obtained from 2DV CFD model based on set up from experiment of Yoshmi Goda, 1966

An observation, based on the figure 2.28, is that the maximum pressure exerted by the wave on the structure does not occur at the wave crest but precedes it. This behavior is attributed

to the fact that dynamic pressure is primarily driven by the acceleration of water particles, which reaches its maximum during the upward rise of the surface elevation. When the wave crest reaches the wall, the vertical velocity of the water particles approaches zero, causing a reduction in the dynamic pressure exerted on the wall.

The observation that the maximum pressure is acting on a structure prior to the peak in water surface elevation taken into account in further analysis in this study.

2.9.2. 2DV based on St. Petersburg case

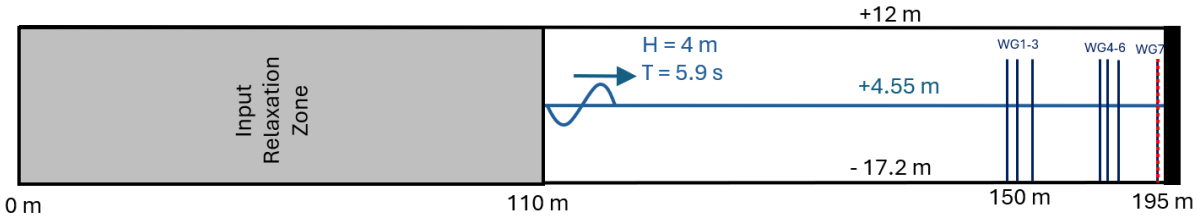

Figure 2.29: The set-up of the St. Petersburg 2DV CFD model. Wave gauges are indicated by WG lines. The red dots indicatethe location of the pressure sensors, which were placed every 0.5 m from -16 to +7.5 m

The set-up for the St. Petersburg 2DV case is the basis for the 3D case. The set-up for this model is schematized in Figure 2.29 The hydraulic condition that is being tested is the basic hydraulic condition with a wave height of 4 m and a period of 5.9 s (presented in the main case in Table 2.1). From this follows the wavelength of approximately 55 m. The water level is at +4.55 m, as described in the case study.

The set-up for this case follows the principles of JIP suggestions as well as the previous case. The inlet relaxation zone is set up to be 2 wavelengths long, and the distance between the inlet relaxation zone and the outlet is chosen to be 1.5 wavelengths. The height of the numerical flume is 29.2 m. The cell resolution that has been used is 16 cells per wave height.

In terms of measurements, 7 wave gauges were placed, as indicated in figure 2.29. The pressure sensors were placed adjacent to the wall structure. The pressure sensors are equally distributed between -16 and +7.5 m, with a distance of 0.5 m between. This distance indicates the position of the sector gate. The height of the gate is a total of 23.5 m, rising above the mean water level of 7.5 m.

2.9.3. 3D based on St. Petersburg case

Due to limited computational resources, the 3D case was set up with reduced dimensions. Both the relaxation zone and the area in front of the structure were limited to one wavelength of 55 m. Additionally, only a single gate (the Southern gate) was modeled. The reduction of the setup to one gate was compensated with the *symmetryPlane* boundary condition, as described in subchapter 2.4.

In 3D set-up, a different refinement was applied as in the 2DV case, using 12 cells per wave height, because of the limited computational resources. Additionally, identical refinements were applied around the surface water level, set at +4.55 m. Furthermore, one level of refinement was applied around the .stl file, with five adjacent cells refined.

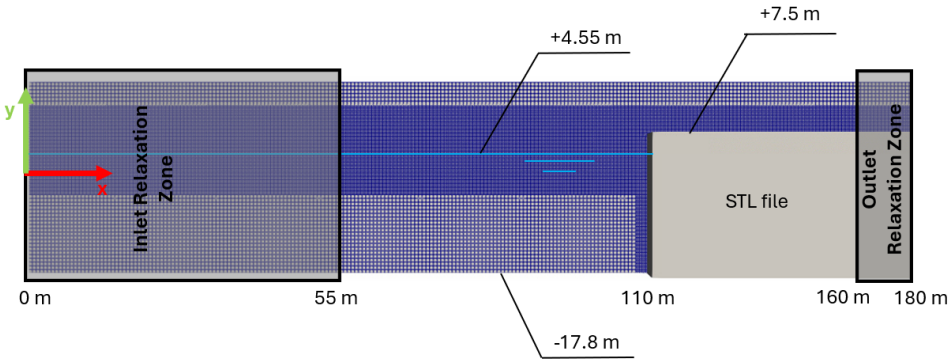

(a) Side view (from *front* patch perspective)

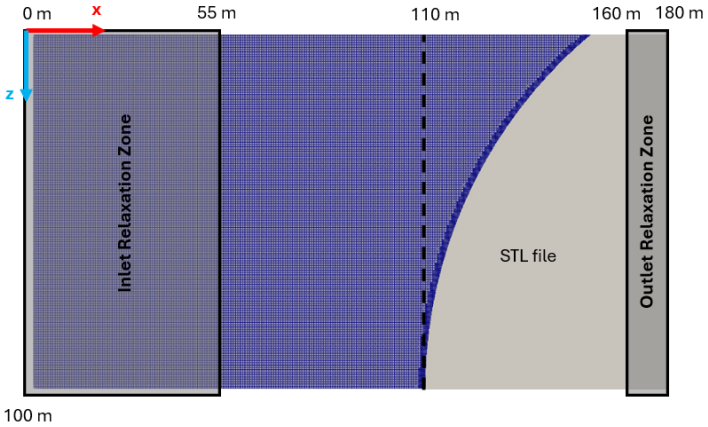

(b) Top view (from *atmosphere* patch perspective)

Figure 2.30: The set-up of the 3D St. Petersburg main case

Along the .stl file representing the gate probes were placed. First, the vertices of .stl file were extracted and then interpolated. Subsequently, probes were positioned along the surface of the structure (.stl file) at intervals of 0.5 m horizontally and vertically between the probes, with a defined distance of 0.35 m normal to the interpolated structure line.

For 9 vertical cluster sets of probe definitions (pressure sensors), wave gauges were placed uniformly along the gate. The set-up of the wave gauge placement in 3D is illustrated in Figure 2.31

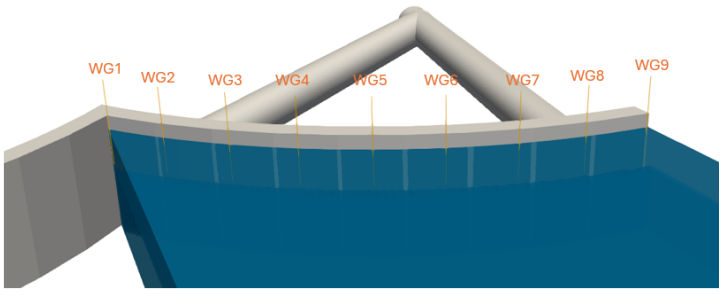

Figure 2.31: The position of the wave gauges along the curvature of the gate in 3D

3

Results

In this chapter, the results of 2DV and 3D simulations for the St. Petersburg cases are presented, corresponding to Step 4 in the Methodology, described in Section1.3. The 2DV results are compared against empirical formulas and linear wave theory. The 3D model is validated using St. Petersburg data. Additionally, this chapter presents an analysis of the 3D data related to Step 5 in Section 1.3. The analysis includes mapping the pressures and fraction coefficient values as well as evaluating the total integrated pressures and their application points.

3.1. St. Petersburg 2DV

From the water elevation time series shown in Figure 3.1, it is observed that the water elevation at the interaction with the wall reaches steady state within the first 50 s of the model run. Analysis of the timeseries indicates that the largest surface elevation at the wall occurs at 240th s. The maximum recorded water elevation at the wall is 6.8 m relative to the Still Water Level (SWL).

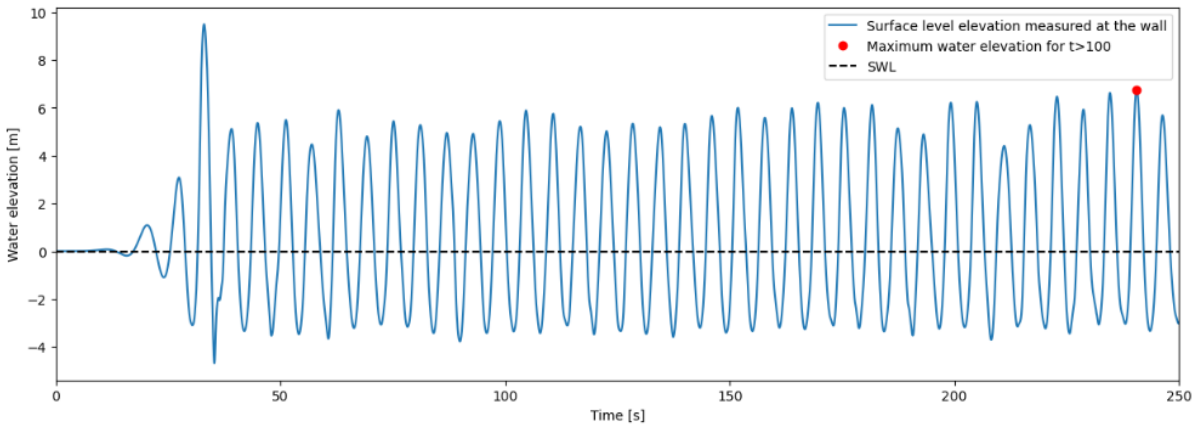

Figure 3.1: Water elevation timeseries for the 2DV St. Peterburg case

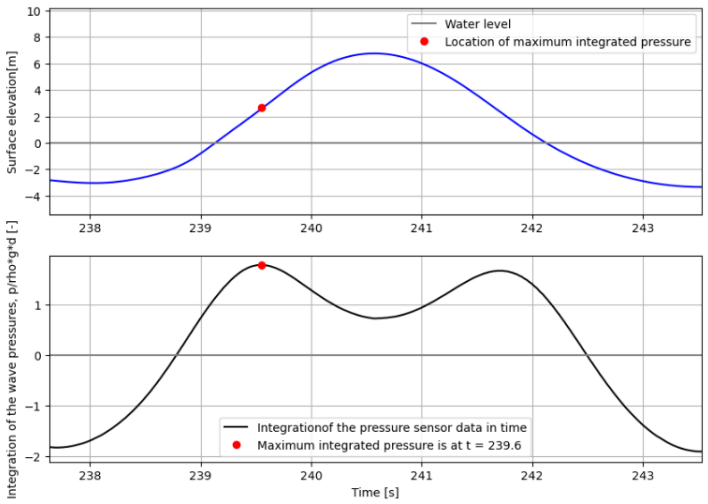

Figure 3.2: Sum of dynamic pressure measurements in time, obtained from 2DV CFD model based on setup of the St. Petersburg case study

In Section 2.9.1, it was concluded that the maximum force acting on the structure does not occur directly beneath the wave crest but precedes it. Consequently, the largest surface elevation at the wall and total integrated dynamic pressure obtained from sensor data were computed and plotted, as shown in Figure 3.2

The maximum pressure was compared to the empirical formulas and the linear wave theory that are described in Chapter 2. This comparison is presented in Figure 3.3. It is evident that the total force calculated with Sainflou empirical formula overestimates the plotted dynamic pressure distribution by approximately 94% compared to the 2DV CFD measurements under the given hydraulic conditions. This difference was calculated by integrating the areas of the plotted results.

Furthermore, the spatial pattern of maximum pressure obtained from the CFD simulation qualitatively resembles the pressure distribution calculated with Linear Wave Theory, although the two do not quantitatively concise. Specifically, at the mean water level, Linear Wave Theory overestimates the forces at the water surface by approximately 58%.

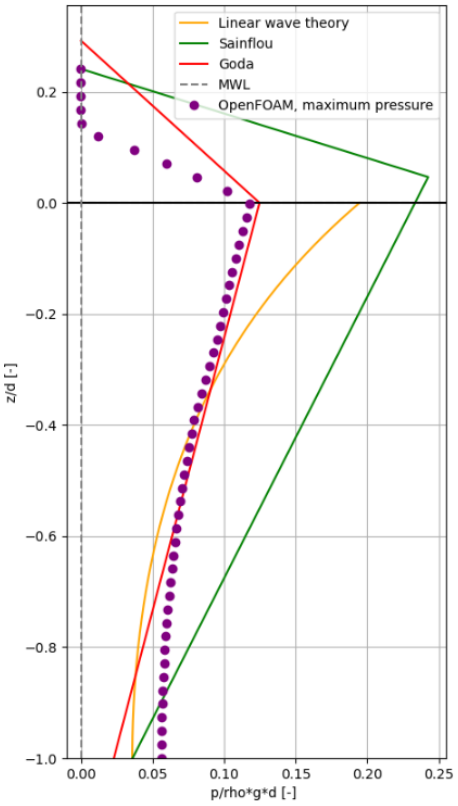

Figure 3.3: The plot of dynamic pressure data recorded by sensors at the moment of time of highest pressure magnitude, and comparison to the empirical formulas and Linear Wave Theory

At the surface level, the maximum measured pressure closely aligns with the maximum pressure calculated using Goda's formula. However, when integrating over the entire depth, Goda's empirical approach overestimates the numerical results by approximately 8%, based on the area between the plotted curves.

3.2. St. Petersburg 3D

Prior to the analytical evaluation of the results, a qualitative comparison was performed between the visual output of the CFD model and an image taken in the physical model tests.

When comparing the images taken in the laboratory to the results of the 3D CFD model at the simulation time of 205 s, it can be observed that the CFD model successfully reproduces a visually similar pattern along the gate, as illustrated in Figure 3.4. At this instance, the overtopping takes place at the junction of two gates in both the numerical model and the physical model test.

At the junction of the gates, the geometry of the gate structure results in significant overtopping at the junction of the sector gates. To quantitatively validate the observed surface elevation at that location, an analysis of he numerically recorded wave gauge data was performed.

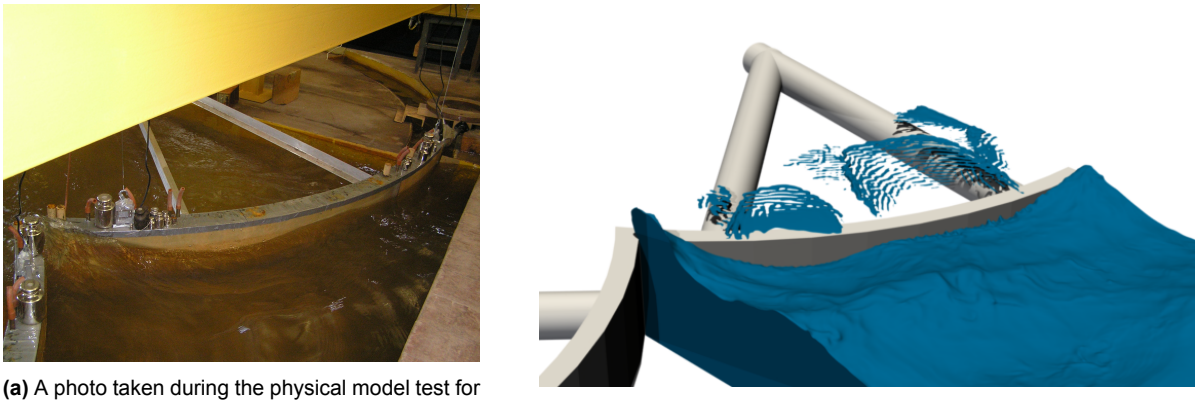

(a) A photo taken during the physical model test for the main case with $0°$ wave incidence at the gate

(b) Snapshot of the numerical 3D simulation at $t = 205s$

Figure 3.4: Visual comparison of physical test and a numerical 3D model

As described in Section 2.6, a symmetry boundary condition was implemented at the gate junction in the 3D model. To qualitatively assess the effectiveness of this configuration, the solution at the time instance of 205 s was mirrored and is presented in Figure 3.5. The qualitative analysis indicates that there are no inconsistencies at the boundary interface between the two gates.

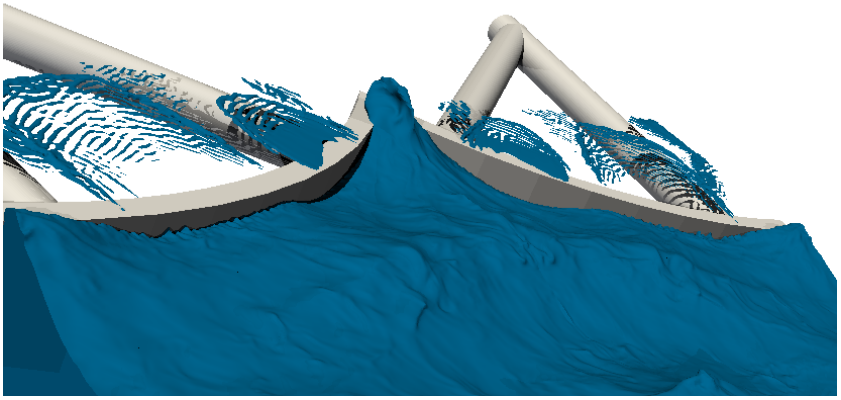

Figure 3.5: Snapshot of the numerical reflected 3D simulation at t = 205 s

Surface elevation analysis at the structure

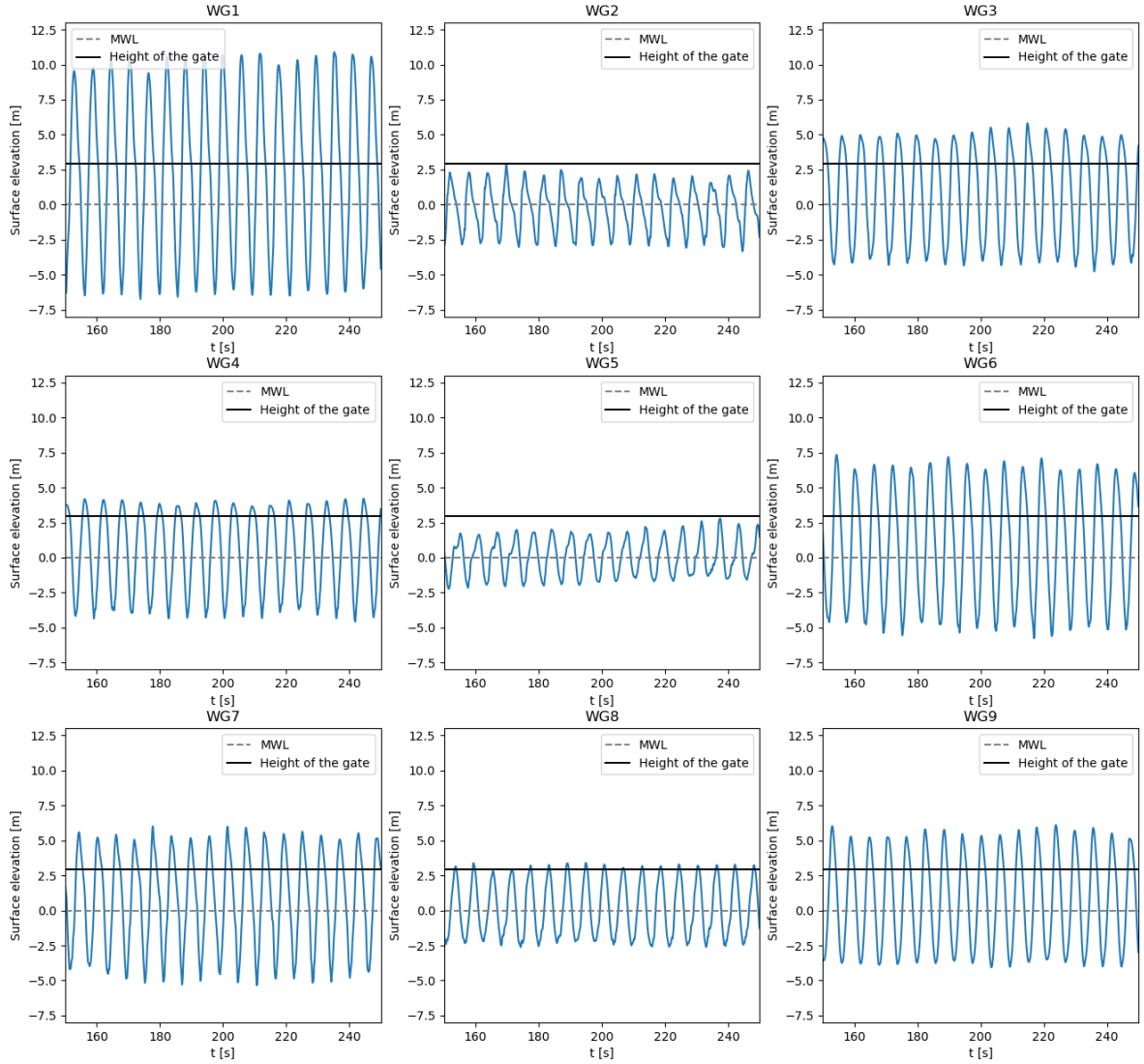

Figure 3.6: Wave gauge numerical data for steady-state water surface elevation in 3D CFD model along the sector gate geometry

The analysis of the wave gauges placed along the gate in the CFD model, as shown in Figure 3.7 and 2.31, is presented in Figure 3.6. This analysis indicates that the wave amplitude at the junction of two sector gates, where the WG1 sensor is positioned, is significantly greater than at the other wave gauge positions. Specifically, the incident wave height entering the numerical domain is 4 m, while at the gate junction, the WG1 wave gauge recorded a wave height of 16 m. It is four times greater than the incoming wave height. These findings suggest that this section of the gate is subject to a large overtopping volume. The presence of this amplified response of surface elevation is due to the geometry of the junction between the two gates. The reflected wave is twice the height of the incident wave, and due to the geometry of the junction, these reflected waves constructively interfere.

Furthermore, the observed spatial variation in the measured water surface elevation suggests that there is a standing wave pattern occurring along the sector gate. Based on this, it can be deduced that WG2, WG3, and WG8 are at or around the nodes, while the remaining wave gauges are at antinodes.

The formation of nodes and antinodes can also be identified from the time-averaged water surface, illustrated in Figure 3.7, where the interface between water and air has been averaged over time and plotted on the surface of the gate. As described in 2.5, the phase fraction coefficient is defined such that a value of 0 corresponds to air and 1 represents pure water. In Figure 3.7, intermediate values between 0 and 1 are clearly visible, and a distinct node-antinode pattern is evident in the mean phase fraction distribution. The locations of the nodes are approximately at 17 m, 55 m, and 90 m from the gate junction.

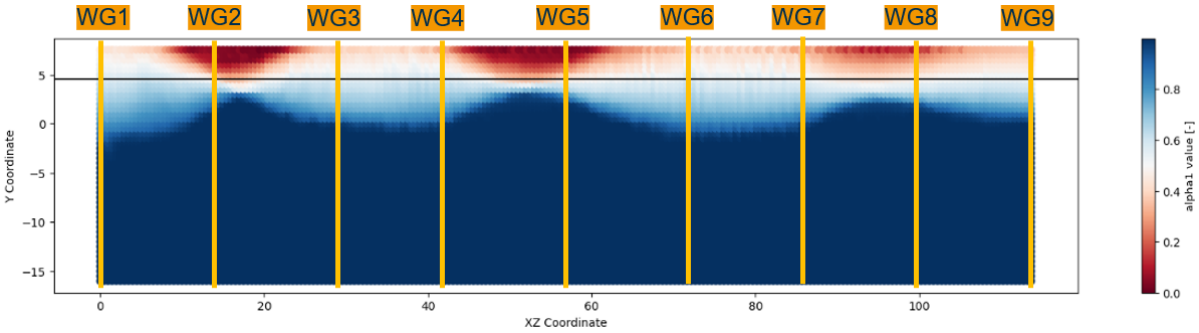

Figure 3.7: Mean values of fraction coefficient (α) measured at the locations of the pressure sensors (probes) in numerical model

Determination of total forces on the surface of the gate

To determine the total force magnitude acting on the gate surface, the pressure time series were measured for each pressure sensor on the surface of the gate and integrated over the area of the leaf gate. In order to isolate the dynamic pressure component, the pressure at timestep 0 was subtracted from each pressure sensor value. This approach was adopted because, in the physical model experiments, the hydrostatic pressure was determined by recording the baseline pressure at the gate prior to initiation of wave action.

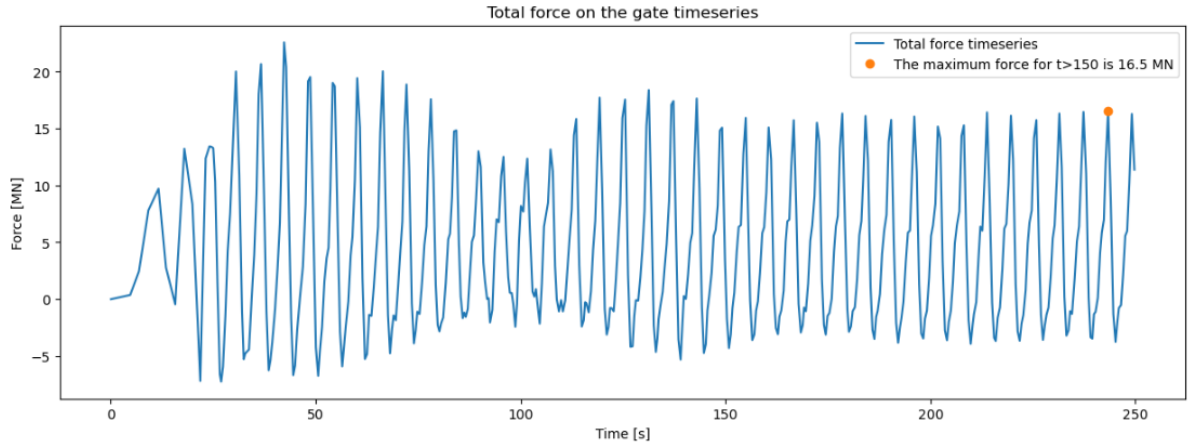

Figure 3.8: Timeseries of integrated force over the gate area

As a result, a time series of the total force magnitude was obtained, as presented in Figure 3.8. As shown in this figure, there are two oscillations in the timeseries before reaching a steady state at 150 s. The nature of the oscillations between 0 and 150 seconds is unknown. One of the factors that could contribute to these oscillations could be an effect of numerical discretizations.

Accordingly, for the subsequent analysis of the numerical simulation outputs, only the steady-state time interval between 150 s and 250 s was considered. The force time series corre-

sponding to this steady-state interval is presented in Figure

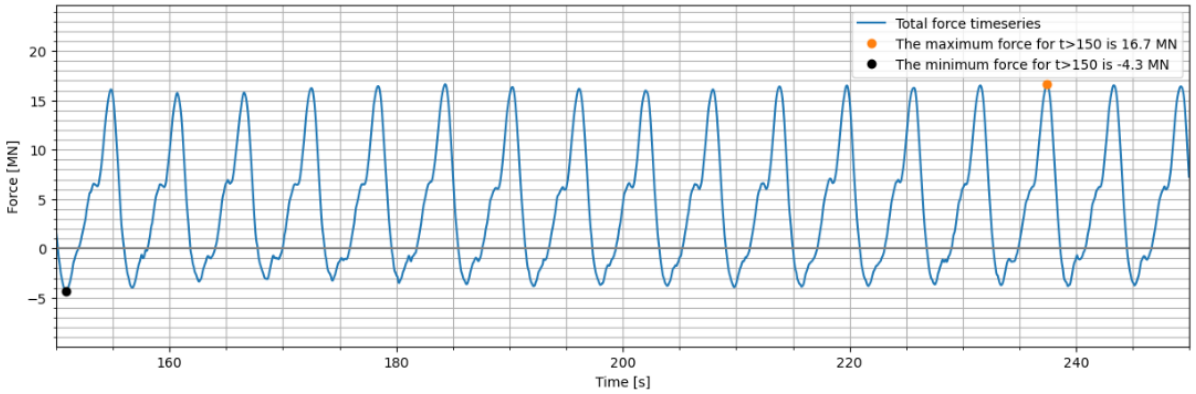

Figure 3.9: Timeseries of integrated force over the gate area when steady state has been reached

The recorded forces represent the magnitudes of the dynamic loads. In the numerical simulations, the computed force magnitude corresponds to the Y-direction force component acting on the support hinge, consistent with the measurements obtained in the physical model. Consequently, the peak dynamic force magnitude obtained from the 3D numerical model is expected to fall within the range defined by the two maximum positive and two minimum negative dynamic force extremes measured on both gates. A comparative analysis of those values is presented in Table 3.1. Based on this comparison, it is concluded that the maximum force predicted by the CFD model, acting in the direction of the barrier's support hinge, lies within the range established by the physical model tests. However, the minimum fore, negative relative to the initial hydrostatic force computed in the CFD model, is approximately half the magnitude of the minimum force recorded in the physical experiments.

	Physical model (F_y) [MN]	3D CFD model [MN]
Maximum	12.2 / 17.0	16.7
Minimum	-9.50 / -16.0	-4.3

Table 3.1: Comparison between the forces acting on the hinge in the physical experiment in the Y-direction and the extreme dynamic force acting on the surface of the gate

Analysis of one period of force timeseries

When closely looked at, the steady state force timeseries, in Figure 3.9, it can be observed that there are three peaks that occur. To investigate the nature of the peaks in the force magnitude timeseries, a one-wave period interval surrounding the maximum measured force at t = 236 s was examined in detail, as presented in Figure 3.10a.

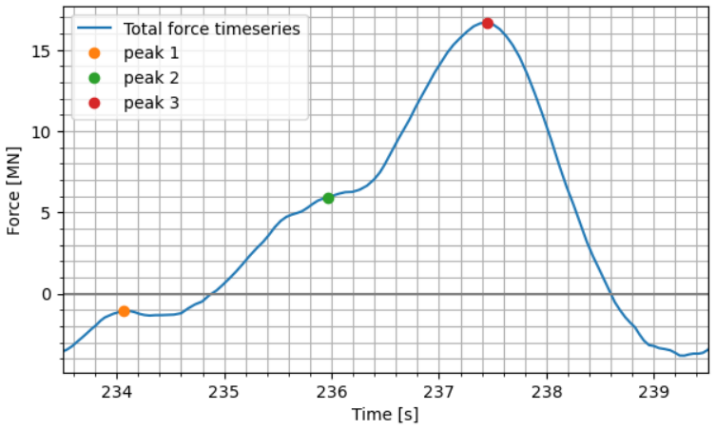

(a) Side view (from *front* patch perspective)n of the peaks in the force magnitude timeseries for one wave period around maximum force observed

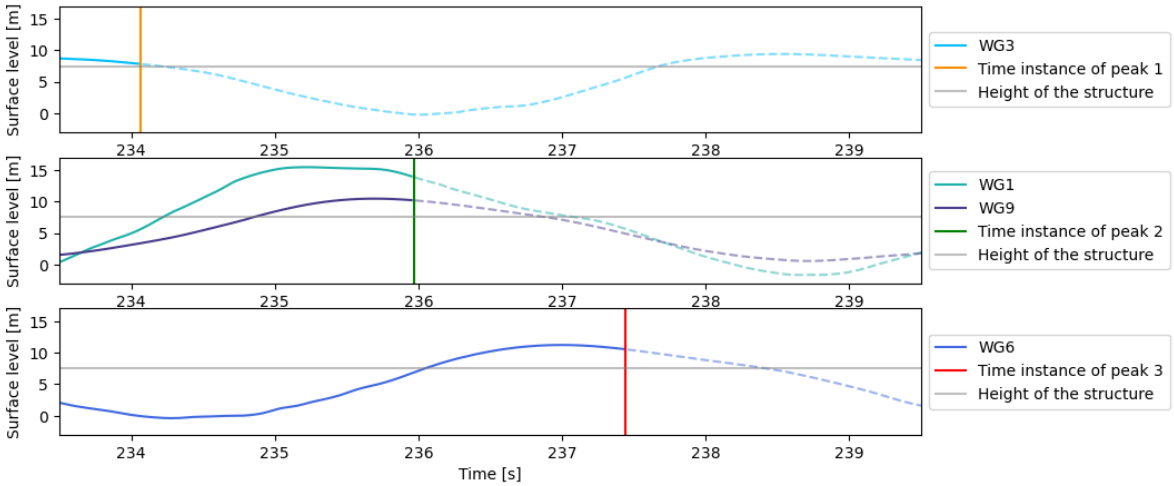

(b) The wave gauge data for wave gauges 1, 3, 6, and 9, located around the overtopping locations of the gate. Sold lines indicate the overtopping prior to peak appearance, dashed line indicates the surface elevation after the relevant force magnitude peak.

Figure 3.10: Force magnitude peaks and their correlation with overtopping in 3D St. Petersburg CFD model

According to numerical data presented in Figure 3.10b, the first peak occurs after overtopping at WG3, which is located at the second antinode from the point of the junction of the gates.

The second peak is observed following overtopping at both ends of the section gate, as measured by the wave gauges WG1 and WG9 and presented in Figure 3.10b.

The third and highest peak occurs when a wave interacts with the central part of the gat, resulting in overtopping at this location. This is reflected in the data recorded by WG6, as shown in Figure 3.10b.

Dominant frequency of the force

In order to analyze the force signal, a Fourier spectrum analysis was performed. Based on the spectrum in Figure 3.11, the significant peaks are observed at 0.17 Hz, 0.34 Hz, 0.51 Hz, and 0.68 Hz, indicating the presence of the second, third, and fourth orders of harmonic components within the force magnitude time series. The spectral analysis identifies a dominant peak at 0.17 Hz, demonstrating that the incident wave energy is primarily concentrated at this frequency. This value corresponds to the frequency derived from the wave period, confirming that the observed spectral peak is associated with the regular wave forcing.

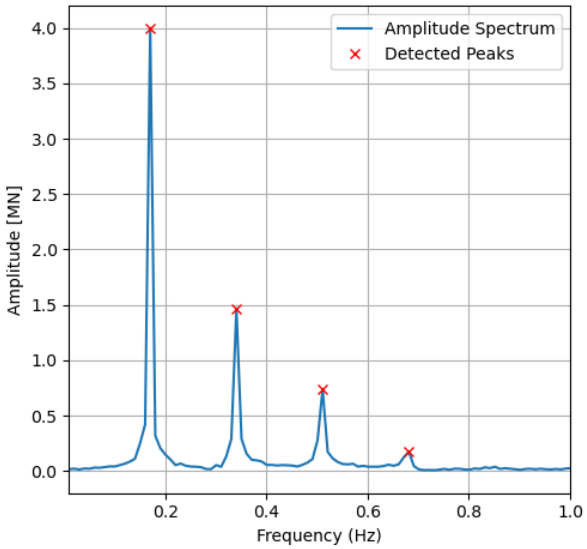

Figure 3.11: Force Spectrum with Peaks

Comparison of 2DV and 3D pressures

The maximum dynamic pressure distribution was computed for the pressure sensors around the antinodes (at WG1, WG3, WG6, and WG9) and around the nodes (at WG2, WG5, and WG8). The data extraction for the pressure sensors followed the same approach used for 2DV pressure distribution: identifying the largest wave height at the pressure sensor's location and selecting a time instance when the sum of the pressure sensor readings is the largest.

From the analysis, it can be observed that the 2DV pressure distribution exhibits larger pressure values than 3D data for the antinodes, as can be observed in Figure 3.12a. A similar conclusion can be drawn from the results of the nodes presented in Figure 3.12b. Based on the calculation of the mean relative difference between 2DV and 3D data, shown in Figure 3.12, it is evident that the 2DV model overestimates the maximum pressure by between 3% and 13% for the antinodes and between 4% and 11% at the node.

An observation that can be made is that for WG9 and WG8, the calculated mean relative difference is 3% and 5%, respectively, which are relatively low. This may be attributed to the fact that the waves at these gauges are normally incident on the gate structure, similar to the 2DV case with a straight wall; however, even in this scenario, the 2DV model overestimates the pressures.

Overall, the pressures obtained from the 3D model run are lower than the pressure obtained in the 2DV model, indicating that the 2DV approach tends to overestimate the localized forces on the structure.

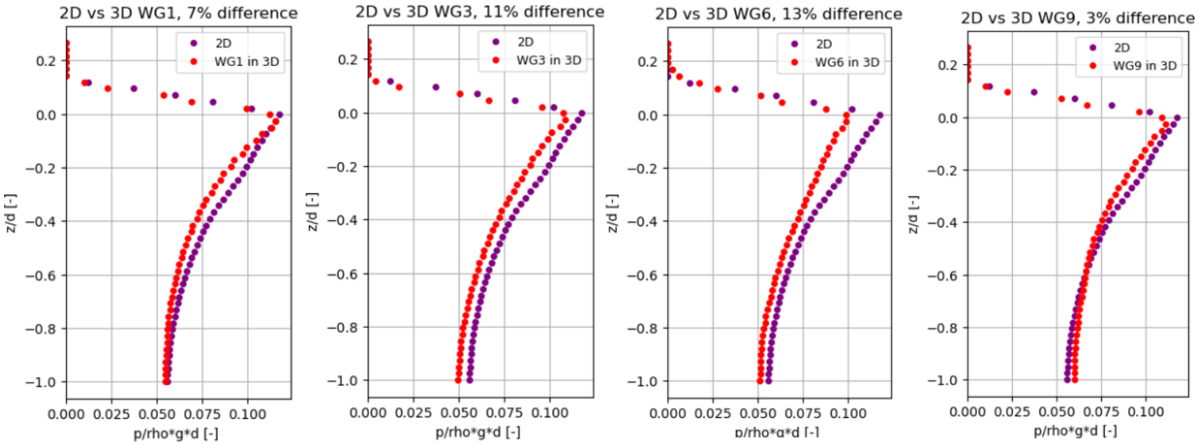

(a) Comparison of the 2DV pressure data to 3D pressure data around locations of the antinodes

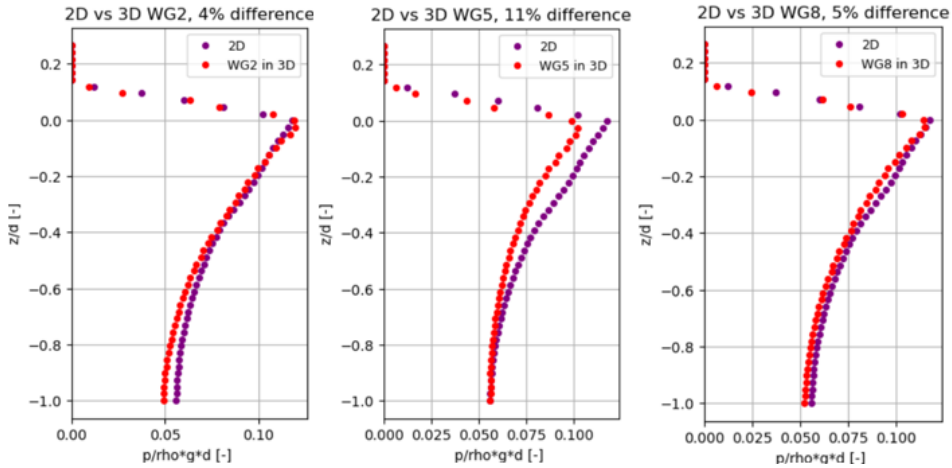

(b) Comparison of the 2DV pressure data to 3D pressure data around locations of the antinodes

Figure 3.12: Comparison of 2DV and 3D pressures. The percentage difference between 2DV and 3D data is calculated using the Mean Relative Difference.

Force application point

Not only does the magnitude of force vary over time, but the point of force application also changes. In Figure 3.13, the locations of wave-induced force application are plotted for one wave period corresponding to the maximum force magnitude. The locations of the application point have been based on formulas presented in Section 2.4. Both application points over the length of the gate leaf and over the height are displayed. The length of the leaf is defined along the *XZ* coordinate.

From the plotted force application points along the curvature if the gate leaf, illustrated in Figure 3.13, it can be observed that prior to peak 3, which corresponds to the largest dynamic force magnitude (after subtracting initial hydrostatic pressure), the application point shifts from the side of the gate toward the middle to a position 70 m from the junction of the gates. After reaching this peak magnitude, the application point moves back toward the side of the gate. Analysis of force application points along the gate leaf indicates that the maximum force occurs at positions between 70 m and 114 m from the gate junction.

From the plotted force application points over the height of the gate in Figure 3.13, it can be observed that the application point of dynamic force predominantly occurs below the mean water level. When the total force magnitude acting on the gate increases, the application

point gradually moves upward until it reaches the mean water level, where peak 2 takes place. Peak 2 is identified as a result of overtopping contributions on the boundary edges of the gate. When Peak 2 occurs, the force application point moves to -7 m relative to the SWL, and subsequently moves upward to the top of the gate by +7.5 m. Peak 1, which is similar to that in Figure 3.10, causes a fluctuation of the vertical application point position around the seabed. First, it rises from the seabed until approximately -7 m relative to the mean water level and then descends. This behavior is very likely a result of the problem being ill-conditioned, as when the computation involves division by quantities that are numerically close to zero, which leads to instability of the result. The ill-conditioned problem also led to the application point values being outside of the defined computational domain, which resulted in missing values in Figure 3.13. In general, the application point is primarily concentrated between the mean sea level and 7 m below it.

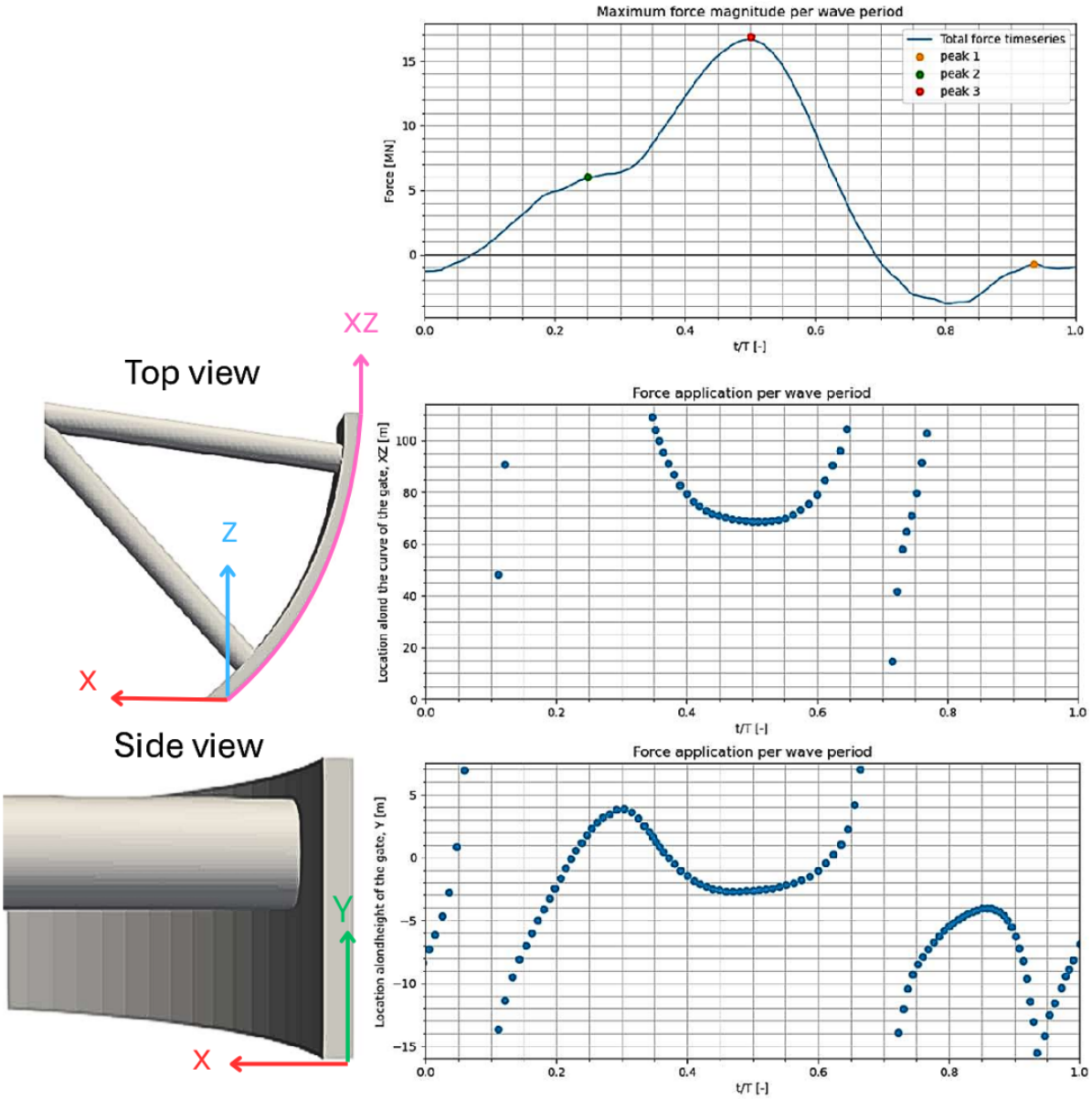

Figure 3.13: Force application points in time. The figure above is the plot of the force magnitudes for one wave period. The plot in the middle shows the application points of the force magnitude over time along the length of the leaf of the gate. The plot below shows the application points of the force magnitude over time along the length of the leaf of the gate.

The force application points time series for vertical and horizontal dimensions, displayed in Figure 3.13, are then combined in the same figure in order to determine clusters of application points. In Figure 3.14, the spatial distribution of force application points occurring on the gate leaf is displayed. The cluster of application points is marked with red dots. By analyzing data presented in Figures 3.13 and 3.14 it is concluded that the most critical point on the analyzed gate leaf is lies within this cluster, not only due to dense concentration of application points in this region, but also because the largest wave force magnitude is observed at this location.

Consequently, based on the spatial and temporal analysis of the force application points, the governing region for extreme forces can be determined. This region is located approximately two-thirds of the way from the junction between the gates.

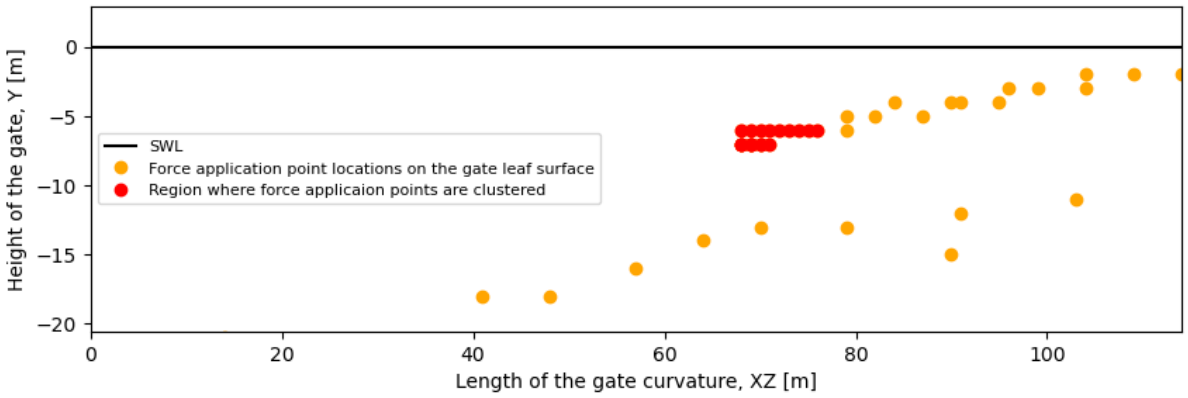

Figure 3.14: All application points plotted over the height and curvature of the sector gate leaf

Mapped pressures

Similar to the calculation of the total force magnitude, a dynamic pressure color map was created by subtracting the initial hydrostatic pressure from the initial time step of the numerical model from the measured pressure values at each time instance. The dynamic pressures are then plotted as a color map. Additionally, the phase fraction coefficient and the total force application point are represented in a plot.

For the time instance t = 236 s, when the maximum dynamic force occurs, the pressures are mapped along with the surface elevation, which is expressed by the map of the fraction coefficient, that traces water elevation at the gate (denoted by *alpha1* values in the plot), which can be seen in the lower plot in Figure 3.15. In this plot, the blue color represents air, and the red color represents water. According to the pressure map in the upper plot in Figure 3.15, the maximum pressure occurs when the wave makes contact with the structure between 55 and 110 m. This can be observed in both the probe data map and the fraction coefficient map.

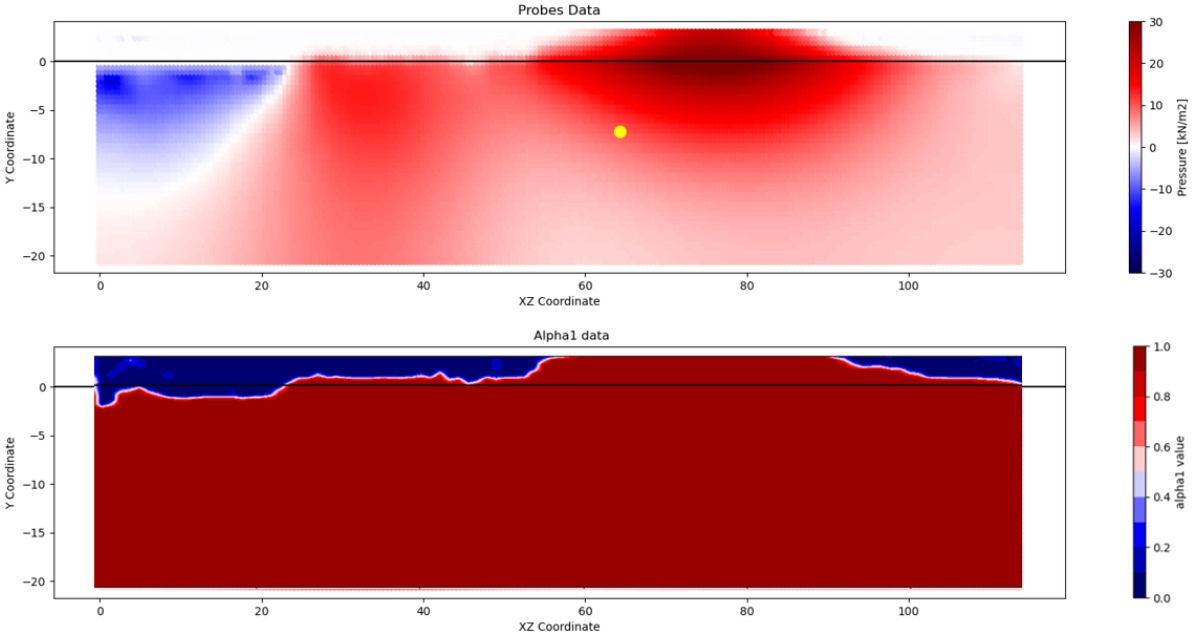

Figure 3.15: The pressure sensors and fraction coefficient data for the time instance of maximum force magnitude. In the ”Probe data” upper plot, the dynamic pressure values are represented, and the lower plot, ”Alpha1,” represents the fraction coefficient values. The black line in the plots indicates the SWL. The yellow dot on the probe data map indicates the application point of the force acting on the gate.

It is observed in Figure 3.15 that a significant pressure concentration occurs around two-thirds of the gate length (with the junction of the gates as reference). However, in the region near the gate junction (between 0 and 20 m), the water level falls below the SWL, which is reflected in negative values in the dynamic pressure distribution on the map.

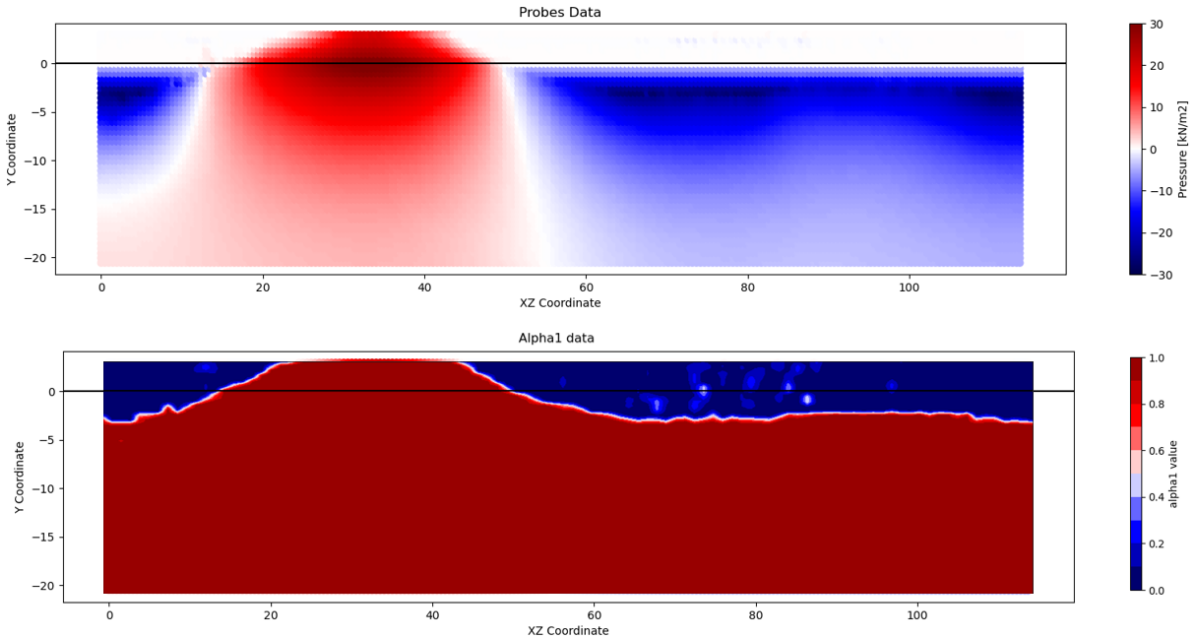

Figure 3.16: The pressure sensors and fraction coefficient data for the time instance of minimum force magnitude. In the ”Probe data” upper plot, the dynamic pressure values are represented, and the lower plot, ”Alpha1,” represents the fraction coefficient values. The black line in the plots indicates the SWL. The black line in the plots indicates the SWL.

Similarly, the analysis of the minimum pressure occurring at the time instance t = 150.9 s was conducted. The pressure map for this time instance is illustrated in the upper ”Probe data” map in Figure 3.16. According to this map, the largest negative values for the dynamic pressures occur when the wave is in contact with the structure between 10 and 55 m on the XZ axis, as can be seen in the ”Alpha1” fraction coefficient map. At this instance, the rest of the gate has water surface level below the SWL, which reflects in negative dynamic pressures measured in the numerical model.

Mean and standard deviation of mapped pressures

The mean of dynamic pressures calculated over time for each pressure sensor is illustrated in Figure 3.17. What stands out in the mean pressure map is that the pattern of nodes and antinodes can be observed. The greatest wave loads typically occur at four distinct locations along the length of the gate: at 0 m (around the junction of two gates), around 35 m, 75 m, and at 114 m.

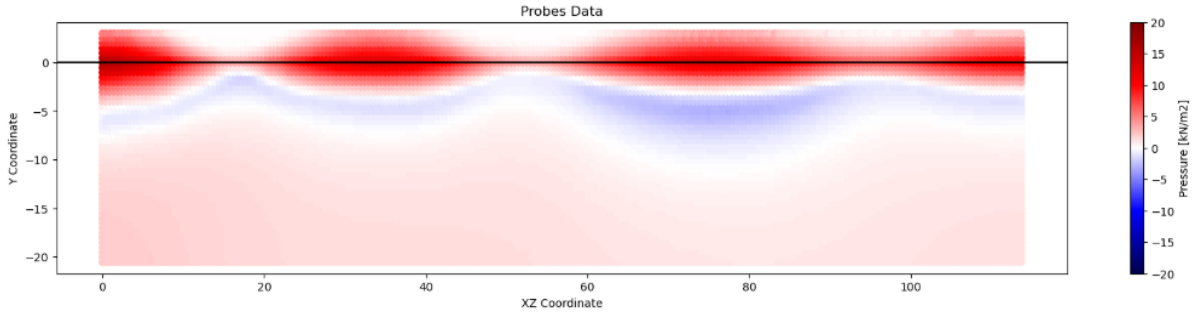

Figure 3.17: The mean dynamic pressures calculated over time map

When examining the standard deviation map of the dynamic pressure (Figure 3.18), it can be observed that the highest standard deviation values are identified in the middle of the antinodes of the mean map. This implies that at the locations of antinodes along the gate leaf, both the greatest variations in force and the highest force values are expected. At the nodes of the maps (in Figure 3.17 and 3.18), the force variations exhibit minimal amplitude, and the corresponding mean pressure magnitudes are also comparatively low.

Based on the analysis of mean and standard deviation, it can be determined that significant pressure fluctuations occur near both ends of the sector gates (0 and 114 m), as well as around 35 and 75 m for the given hydraulic conditions, bathymetry, and sector gate.

The concentrated cluster (or antinode) of mean forces is between 0 and 20 m, which corresponds to the location of the junction of two gates. According to Figure 3.18, the largest pressure fluctuations are expected in this location.

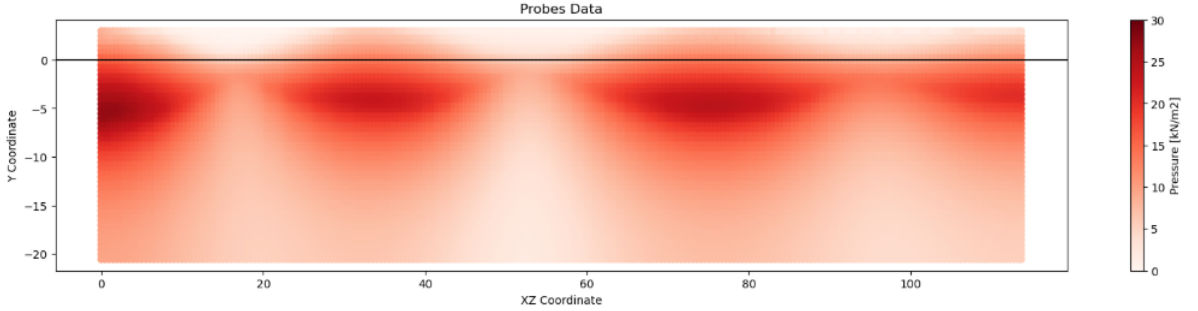

Figure 3.18: The standard deviation map of the dynamic pressures calculated over time

Based on the mean water level map of the phase fraction coefficient α, the nodes along the sector gate can be defined as illustrated in Figure 3.19.

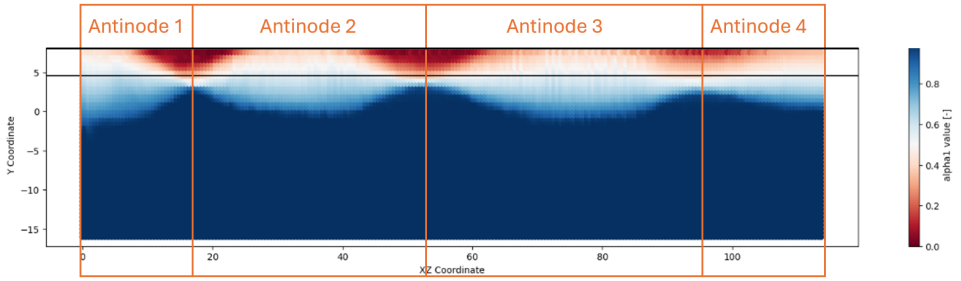

Figure 3.19: Definition of antinodes on the mean fraction coefficient map

For each wave antinode, the time series are plotted in Figure 3.20. The order of magnitude of the force magnitudes should not be directly compared, because the antinodes have different areas. It can be observed that for Antinode 1, the highest peak is four times larger than the second peak. No similar behavior is observed in the remaining wave antinodes.

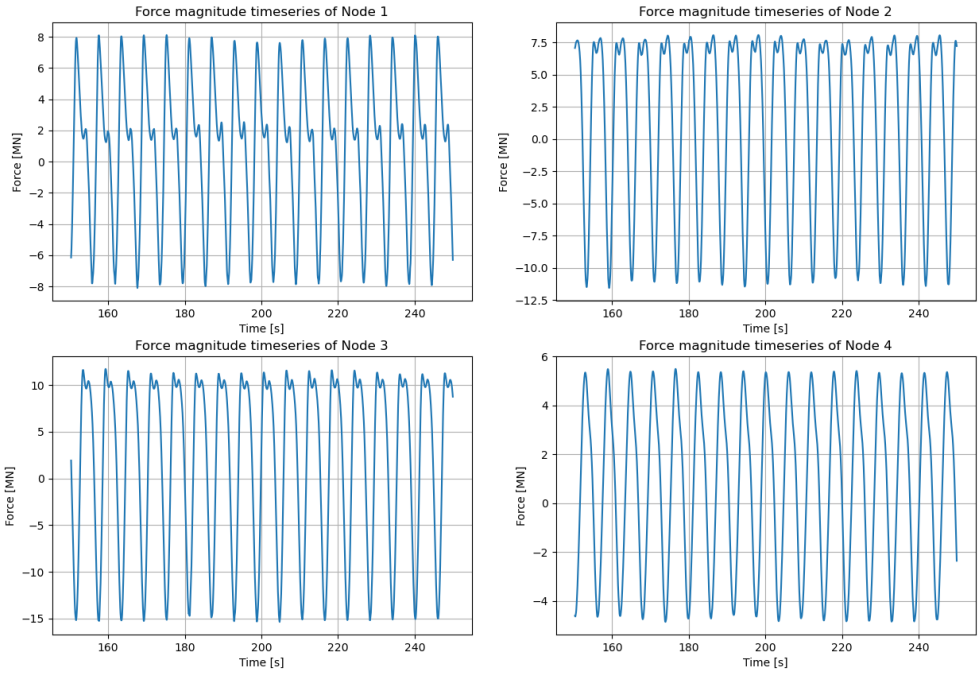

Figure 3.20: Dynamic force magnitude timeseries plotted for each antinode

The phase difference between the antinodes was calculated from the force magnitude timeseries at each antinode. In the analysis of the phase differences in the force magnitude timeseries for the wave antinodes along the gate leaf, the phases were calculated relative to Antinode 1, which is located at the junction of the gates. The analysis was done for the stationary part of the force timeseries, starting with t = 150 s. The comparison of the plotted force magnitude of antinodes to antinode 1 can be found in Appendix B.

From phase differences analysis, results of which can be seen in Table 3.2, it can be observed that the Antinode 2 is leading Antinode 1 by $130°$, Antinode 3 is lagging Antinode 1 by $118°$

and Antinode 4 is lagging by $47°$. This suggests that there is a sharp phase transition between Antinode 2 and Antinode 3, which suggests that the forces acting at these antinodes may contribute to the torsion of the gate leaf.

Nodes compared	Phase difference at dominant frequency [degrees]
Node 1 and 2	129.53
Node 1 and 3	-118.19
Node 1 and 4	-47.81

Table 3.2: Phase differences between the standing wave nodes along the gate leaf

4

Discussion

4.1. Performance of the CFD model

When comparing the performance of the 2DV model to the experimental study of Goda (1996), the numerical results exhibited a strong correlation with the physical test outcomes. However, it was not possible to precisely quantify the accuracy of measured forces by the numerical model, as the experimental data of Goda was extracted from published figures rather than obtained as raw numerical values. Despite this, both visual comparison and overall trend alignment indicate that the numerical model reliably captures the order of magnitude of the measured pressures for time instances under wave crest, trough, and the maximum pressure acting on a wall. Furthermore, the time series of pressure data recorded by individual pressure sensors in the numerical model demonstrated a good agreement with experimental results.

The additional observation from the numerical model results was made that in the case of the standing waves under regular wave conditions within the 2DV framework, the maximum wave force does not coincide with the wave crest at the wall. The maximum force occurs before the highest surface elevation at the wall is reached, because the acceleration contributing to the dynamic pressure component is greater prior to the crest.

Based on the conclusions drawn from analyzing a numerical case based on Goda's experiments, the St. Petersburg hydraulic conditions and water depth were used to evaluate the pressure induced on the wall in the 2DV case. This study demonstrates the consistency of the numerical pressure data with the Goda empirical formula. However, findings suggest that while the empirical formula of Goda approximates overall force trends well, it tends to overestimate the forces acting on the vertical wall in the 2DV model. The analysis also shows that the Sainflou method overestimates the numerical 2DV results by 94% and the quasi-linear Linear Wave Theory overestimates them by 54%. This indicates that he numerical analysis of forces exerted on a structure can contribute significantly to the structural design optimization, as it provides more realistic force estimations than empirical formulas and the quasi-regular Linear Wave Theory.

Building upon the 2DV case, the study was extended to a 3D case where a more complex structure was implemented in place of the wall. For the 3D case, the order of magnitude of extreme positive forces aligns well with physical tests, with the extreme maximum dynamic force reaching 16.7 MN, while the physical experiments indicate this value lies between 12.2 MN and 17.0 MN. However, the negative forces were not well reproduced, as it is two times smaller than the expected value. During the physical model tests of the sector gates, the forces were not measured directly at the surface of the gate leaves with pressure sensors, but rather at the gate supports (hinges), representing the structural response to applied forces rather than direct surface measurements on the gate leaves. Moreover, the rigid gate structure was tested in the physical model was placed in a hanging position and not resting at the bottom.

Also, in the physical model, the water level was present on both sides of the gate, a condition that was not replicated in the numerical model.

As a result, the precise accuracy of the results obtained from the 3D model data presented in this study cannot be fully validated. Despite this limitation, the maximum force obtained in the numerical model falls within the expected range, as measured on the hinge of the sector gate. Additionally, the global patterns of the wave-structure interaction observed in the result analysis of the numerical model output are consistent with theoretical expectations; for example, the largest forces occur on the part of the gate where waves are more normally incident. At the junction of the gates, the measured wave height is four times larger than the incoming wave height due to the reflection of both gates at the junction.

4.2. Capabilities and practical considerations of 3D CFD model

In general, the method of analyzing the 3D data presented in this study provides valuable insight into the wave behavior around the sector gate for the specific wave condition that was analyzed. This method demonstrates a possibility to extract highly detailed data for extreme wave conditions, providing insight into the areas in the gate that are most affected by wave interaction. This analysis has shown that the model is capable of simulating waves in 3D and includes complex structure geometries, such as sector gates. The results of the CFD 3D model are able to identify critical areas within a structure. Based on these findings, the further evaluation of the structural response can be undertaken. For example, from the knowledge base within DHV, when the St. Petersburg gate was designed, the maximum force acting on the gate was equally distributed between the two supporting arms of the gate. However, from this study, it can be observed that the maximum force occurs with the application point shifting between the side of the gate and approximately two-thirds along the gate, indicating that when extreme force occurs, one supporting arm of the gate may experience a significantly higher dynamic load than the other. Such observation should be considered in the future design or redesign of the sector gate.

Therefore, the numerical 3D model is able to provide extensive measurement data when properly set up. An experienced modeller can set up the model within a day; however, the computation times of the model are very long. Running one 3D model in this study required 2.5 weeks and occupied 846 GB of memory. Compared to physical tests, the numerical model offers a higher spatial and temporal resolution, providing insights that are more challenging to obtain in physical experiments. Setting up a physical model generally takes weeks and incurs high costs, which represents a significant disadvantage of physical model testing. However, once the setup is completed, multiple wave conditions can be tested and evaluated, using the same setup, allowing the data collection of a large dataset for various wave conditions within a relatively short period.

This study shows that the grid adjustments in the numerical model are necessary to account for wave height and length variations. Additionally, modelling the obliquely incident waves presents additional challenges, as a literature study of grid quality shows that misalignment between grid cells and flow direction can result in significant numerical diffusion. In addition to the need to set up a new model grid for each hydraulic condition, each model run takes a very long time for 3D cases.

Next to the CFD model, physical modelling and empirical relations, other numerical models exist as well, such as mild-slope models. In order to compare the applicability of these methods, comparison to CFD is presented in Table 4.1. In this comparison, it is concluded that the most accurate methods are physical modelling and 3D CFD modeling. However, the most

efficient method is empirical modelling, which can be used for a fast feasibility check at the preliminary stage of design. Furthermore, SWASH can be used; however, when compared to OpenFOAM, SWASH is less suitable for applications where force impulse is critical. Therefore, OpenFOAM models are recommended for such cases (Gruwez et al., 2020).

	Efficiency	Accuracy	Phenomena	Application
Empirical formulas	++	-	Wave run-up, overtopping, pressures	Quick feasibility check
CFD 2DV	+	+	Wave run-up, overtopping, pressures, wave breaking	Design optimization, critical cross-section evaluation
CFD 3D	- -	++	Wave run-up, overtopping, pressures, wave breaking, 3D wave propagation (incl. refraction, diffraction etc)	Final detailed design, validation for selected cases
Physical models	-	++	Wave run-up, overtopping, pressures, wave breaking, 3D wave propagation (incl. refraction, diffraction etc)	Design optimization, final design validation, critical safety cases
Mild slope models	+	-	Wave propagation, refraction, diffraction	Wave transformation up to hydraulic structure, conceptual and preliminary design
SWASH	+	+	Non-linear wave transformation, wave breaking, run-up, wave-structure interaction	Detailed design

Table 4.1: Comparison of the methods for the wave-structure interaction on accuracy, efficiency, modeled phenomena, and suggestions for applications of the methods

Therefore, while implementing the CFD numerical model for analyzing the forces acting on hydraulic structures offers many advantages over the physical model, physical models remain more practical when multiple hydraulic conditions need to be tested. In practice, a combination of both approaches is recommended because with the physical model, the governing hydraulic case can be identified. Once the main hydraulic case is identified, it can be further evaluated using the CFD model in order to gain detailed insights into the processes occurring in the system.

4.3. Limitations

Avaliable computational power

As previously mentioned, one of the major limitations of using the CFD method for analyzing the sector gate structures is the model size. Modeling two gates, rather than one, would require significantly more computational power than is available. In this 3D case study, for example, running a model with a slightly coarser grid of 12 cells per wave height, a total of around 7.3 million cells, and including only one gate with no complex bathymetries for 250 s with the regular wave, it requires 2.5 weeks of running time. It appears that modelling a sector gate wider than 100 m under the specifically used wave conditions would be unfeasible with the current setup and computational capacity of 16 cores.

If a case with longer waves were to be analyzed, the size of the numerical flume would have needed to be proportionally increased to accurately model the long waves. This would result in an excessively large number of cells, exceeding the limits of currently available computational power. However, it should be noted that other models, for example, potential flow models, are more suitable for the analysis of long waves, and the primary strength of the CFD model is its ability to model short, steep waves.

Simplifications

Moreover, due to limitations in the number of cells and model size, certain simplifications were necessary. For example, no breakwater and side banks of the challenge were taken into ac-

count. Instead, a fully reflective boundary was applied on the side of the numerical domain. In reality, the channel has revetments which do not have 100% reflection, hence the energy of the waves would have been partially dissipated. In order to introduce an energy dissipation in the model, a relaxation zone could be implemented instead of a fully reflective boundary. However, this would require expanding the computational domain and, consequently, increasing the number of cells in the mesh, which is not feasible, given the limited computational capacity. The gate structure was modeled to be 100% reflective as well. In reality, the structure is not 100% reflective and responds dynamically to wave frequencies; therefore, actual wave-structure interactions result in greater dissipation.

For waves normal to the structure, a symmetrically modeled domain allows for simulating only half of the computational domain. However, if the obliquely incident waves were modeled, the entire domain would need to be taken into consideration. This is due to the fact that if obliquely incident waves were to be modeled, the *symmetryPlane* boundary condition would no longer be applicable. Moreover, if only one of the gates with oblique wave incidence were modeled, the reflection patterns and seiching modes would not be accurately captured in the model.

In reality, there is a gap between the two gates. In the CFD model, no opening was included between the gates, as this would result in modelling very high velocities in the gap. Modelling of such velocities would require significantly smaller grid resolution around the junction of the gates. Since challenges were encountered with configuring *SnappyHexMehs* and the overall computational demands, further mesh refinement around that region would not be feasible. For future studies, it is recommended to include the pressure release at the junction of the gates for more accurate results. This can be done by placing the gap at the junction of the gates or simulating the pressure release by placing porous layers at the junction of the gates.

5

Conclusion and recommendations

5.1. Conclusions

The objective of this study was to evaluate the applicability of the CFD modelling using the OpenFOAM and Waves2Foam package for determining the hydraulic loads on storm surge barrier sector gates. The relevance of this study lies in addressing the existing research gap in hydraulic loads on complex shapes, such as storm surge barriers, while the demand for the design and installation of sector gates rises worldwide.

Therefore, this study answers the following question that was posed in Chapter 1:

How can 3D Computational Fluid Dynamics (CFD) modeling be utilized in order to analyze the spatial distribution of wave-induced pressure on storm surge sector gates?

In order to answer this research question, three CFD models were set up and their results analyzed. The first model, set up in 2DV, was used to validate the pressure distributions against the physical model results of Goda (1966). The second 2DV model was set up based on the hydraulic conditions of the physical model of the St. Petersburg sector gate. Its results were compared with the theoretical and empirical calculations of pressure distributions. Finally, the 2DV case-study model was extended into a 3D model, with its outcomes initially compared to the outcomes of physical model tests, followed by extensive analysis of the pressure distribution over the sector gate.

The results of the 2DV case, based on Goda's physical model test, demonstrated an overall trend alignment in both spatial pressure data and temporal pressure fluctuations per sensor over one wave period. In the second 2DV case, based on the St. Petersburg cross-section, developed with a resolution of 16 cells per wave height, and extreme hydraulic conditions of the case study with wave height of 4 m and period of 5.9 s, the maximum pressure distribution aligned with empirical relations of Goda, however, the empirical formulas of Goda overestimated the result by 8%. The 2DV numerical result displayed a profile similar to the Linear Wave Theory; however, the Linear Wave Theory overestimated the CFD 2DV model results by 54% at the maximum pressure measured at the mean water level. The Sainflou empirical method overestimated the 2DV results overall by 94%, which makes it the least suitable approach. Overall, the 2DV CFD model demonstrates that both the empirical formulas and Linear Wave Theory overestimate the forces exerted on a wall of a structure.

In the 3D model of the St. Petersburg sector gates, an optimal resolution of 12 cells per wave height was used as a trade-off between accuracy and available computational power. Furthermore, the numerical flume length was reduced, and the model was restricted to a single gate due to limited computational resources available. The analysis of the data recorded by the numerical wave gauges in the 3D CFD model along the gate reveals that at the junction of the gates, the wave height is approximately four times larger than the incoming waves, which

is a result of the shape of the gate and the model simulating reflection from both gates. In the results of pressure measurements obtained from the 3D CFD model, the largest peak of maximum total forces was measured as 16.7 MN, falling within the range of 12.2 MN to 17 MN, as measured during the physical tests. In contrast, the negative extreme forces were underestimated by roughly two times. The forces measured in the CFD model showed three peaks in the force magnitude. These peaks occurred after the overtopping events at the junction of the gates, near the junction of the gates, and at the location approximately two-thirds away from the junction of the gates. The latter location corresponded to the highest measured pressures and the application points of the largest total forces.

The analysis of the spatial and temporal pressure variations on the tested sector gate under a single hydraulic condition revealed the formation of four antinodes along the gate. At these antinodes, the maximum localized pressure occurred, as well as the greatest temporal variation of it. Furthermore, there was a sharp phase transition between two antinodes in the middle section of the gate, which is a critical feature that has to be taken into account while designing a sector gate.

In conclusion, this study demonstrated that CFD modelling can effectively estimate the spatial distribution of pressures on storm-surge barrier gates. The analysis of data from the numerical model showed that in 2DV, the pressure distributions were in agreement with theory and physical experiments. In the 3D numerical outcomes, the measured values fell within the expected range, which was measured in the laboratory. However, the negative extreme forces were underestimated. Notably, the analysis of 3D CFD model data was able to identify the maximum forces acting on a gate and the application points of the largest forces, which can be used in the design of the support arms of the structure. The CFD-based approach provides insights into the magnitude and critical location of design forces on the structure, while also enabling the identification of the type of forces and the locations of significant forces, averaged over time. For a provided case study, the analysis revealed four critical locations at four antinodes along the gate. These findings from the 3D CFD model offer valuable insights for designing and optimizing the sector gates in the future.

5.2. Recommendations

For design of the gate

In terms of applying the results of the developed model in practice, the analysis providing the value of total force can be used for determining loads on the gate in the closed state. The spatial force analysis is recommended for determining the load on the supporting arms of the gate, as it seems that the dynamic load on the gate is not symmetrically divided between the arms. The application point along the vertical axis can also be used for calculating the possibility of the gate structure experiencing upward force if the gate shape has curvature over the height of the gate. Furthermore, the analysis of the node-antinode formation and phase calculation within the antinodes is recommended for assessing the torsion of the gate leaf.

The developed model is very large; therefore, it is recommended to use the analysis above only for the detailed design validation. To broaden the model's application in the preliminary design stage of large structures, optimizations are needed in order to reduce the computational time.

For 3D numerical modelling

The 3D model setup faced a number of limitations related to the high computational resources required, which restricted the size and resolution of the model. Currently, this 3D model should

be mostly used for the evaluation of the final design. In order to make this model applicable for earlier stages of the design process, for future studies, it is recommended to investigate methods for reducing the number of computational cells in 3D CFD modeling. One of the methods could be the use of a one-phase CFD model. In this study, the two-phase model was implemented, resolving both air and water. Future research can assess the applicability of one-phase models, which resolve only the water phase, while estimating forces on storm surge barriers or other complex structures.

Furthermore, the forces and pressures estimation in this study was done based on the load of regular waves, which were based on $H_1\%$. Therefore, it is recommended to perform an irregular waves run. In order to obtain the wave statistics for identifying the highest waves that can occur, and determining governing extreme load combinations on the sector gate structure.

In this study, the side boundary was defined as the no-slip boundary, which is a fully reflective boundary condition. In order to develop a model closer to reality, porous layers or outlet boundaries can be considered on the side boundary. However, this should be carefully implemented, as it leads to an increase in the size of the numerical model.

Lastly, the investigation of the loads on the sector gates can be further extended by modelling the sector gate as a floating object. This approach would add insights into the sector gate movements as the hydraulic forces act on it.

References

Ahmed, M. A., Sridharan, B., Saha, N., Sannasiraj, S., & Kuiry, S. N. (2022). Assessment of coastal vulnerability for extreme events. *International Journal of Disaster Risk Reduction*, *82*, 103341. https://doi.org/https://doi.org/10.1016/j.ijdrr.2022.103341

Chenlong. (2025). The finite volume method (fvm). https://www.math.uci.edu/~chenlong/226/FVM.pdf

Dircke, P., Jongeling, T., & Jansen, P. L. M. A global overview of navigable storm surge barriers. In: 2012, November, 150–169. ISBN: 978-0-7844-1252-7. https://doi.org/10.1061/9780784412527.011

Engsig-Karup, A., Bingham, H., & Lindberg, O. (2009). An efficient flexible-order model for 3d nonlinear water waves. *Journal of Computational Physics*, *228*(6), 2100–2118. https://doi.org/https://doi.org/10.1016/j.jcp.2008.11.028

Gamet, L., Scala, M., Roenby, J., Scheufler, H., & Pierson, J.-L. (2020). Validation of volume-of-fluid openfoam® isoadvector solvers using single bubble benchmarks. *Computers & Fluids*, *213*, 104722. https://doi.org/https://doi.org/10.1016/j.compfluid.2020.104722

Goda, Y. (1967). The fourth order approximation to the pressure of standing wave. *Coastal Engineering in Japan*, *10*, 1–11.

Greenshields, C. J. (2024). *Openfoam v12 user guide*. CFD Direct.

Gruwez, V., Altomare, C., Suzuki, T., Streicher, M., Cappietti, L., Kortenhaus, A., & Troch, P. (2020). An inter-model comparison for wave interactions with sea dikes on shallow foreshores. *Journal of Marine Science and Engineering*, *8*(12). https://doi.org/10.3390/jmse8120985

Hunter, P. (2012). The st petersburg flood protection barrier: Design and construction. la barrière de st petersburg : Conception et construction. *33èmes Journées de l'Hydraulique Grands Aménagements Hydrauliques Enjeux Sociétaux, Bénéfices Economiques et Innovations Techniques 14 - 16 novembre 2012. 2012.* https://www.persee.fr/doc/jhydr_0000-0001_2012_act_33_1_1216

Jacobsen, N., Fuhrman, D., & Fredsøe, J. (2012). A wave generation toolbox for the open-source cfd library: Openfoam®: Wave generation toolbox. *International Journal for Numerical Methods in Fluids*, *70*(9), 1073–1088. https://doi.org/10.1002/fld.2726

Kamphuis, J. W. (2020). *Introduction to coastal engineering and management* (Vol. 48). World Scientific.

Kortenhaus, A., Oumeraci, H., Allsop, W., Mcconnell, K., Gelder, P., Hewson, P., Walkden, M., Müller, G., Calabrese, M., & Vicinanza, D. (2001, February). Wave impact loads - pressures and forces.

Kozin, D. (2024). St. petersburg's dam is holding back the floods, for now [Retrieved from https://www.themoscowtimes.com/2019/02/21/st-petersburgs-dam-is-holding-back-floods-for-now-a64066]. *The Moscow Times*.

Liang, X., Zhang, Q., Huang, W., Dai, Z., & Cai, J. (2024). Experimental and numerical study on static performance of ship lock sector gates. *Journal of Constructional Steel Research*, *222*, 108977. https://doi.org/https://doi.org/10.1016/j.jcsr.2024.108977

Lintermann, A. (2021). Computational meshing for cfd simulations. In K. Inthavong, N. Singh, E. Wong, & J. Tu (Eds.), *Clinical and biomedical engineering in the human nose: A computational fluid dynamics approach* (pp. 85–115). Springer Singapore. https://doi.org/10.1007/978-981-15-6716-2_6

Marques Machado, F. M., Gameiro Lopes, A. M., & Ferreira, A. D. (2018). Numerical simulation of regular waves: Optimization of a numerical wave tank. *Ocean Engineering*, *170*, 89–99. https://doi.org/https://doi.org/10.1016/j.oceaneng.2018.10.002

Mata, M. I. (2021). *Numerical estimation of wave loads on crest walls on top of rubble mound breakwaters using openfoam* [Master's thesis, TU Delft]. https://repository.tudelft.nl/record/uuid:36b66c90-dfdb-41d0-b1f2-1253d3f87b4c

Mingham, C., Qian, L., & Causon, D. (2016). Chapter 6 - computational fluid dynamics (cfd) models. In M. Folley (Ed.), *Numerical modelling of wave energy converters* (pp. 105–122). Academic Press. https://doi.org/https://doi.org/10.1016/B978-0-12-803210-7.00006-2

Mooyaart, L., Jonkman, S., de Vries, P., Toorn, A., & Ledden, M. (2014). Storm surge barrier: Overview and design considerations. *Coastal Engineering Proceedings*, *1*, 45. https://doi.org/10.9753/icce.v34.structures.45

Moretto, M. (2020). *An efficient numerical approach to model wave overtopping of rubble mound breakwaters* [Master's thesis, TU Delft]. https://repository.tudelft.nl/record/uuid:2f5bc1a6-160f-47bb-91a8-996c18867221

Ravindar, R., Schimmels, S., Sriram, V., Stagonas, D., & Murthy, M. (2016). Spatial distribution of impact pressure on a parapet using tactile sensors. *PIANC-COPEDEC IX*.

Rijkswaterstaat. (n.d.). Maeslant barrier [Accessed: 2024-09-23].

Stagonas, D., Lara, J. L., Losada, I. J., Higuera, P., Jaime, F., Galani, K. A., Dimas, A. A., Vousdoukas, M. I., Kudella, M., & Müller, G. Large scale measurements of wave loads and mapping of impact pressure distribution at the underside of wave recurves. In: In *Proceedings of the hydralab iv joint user meeting*. 2014. https://api.semanticscholar.org/CorpusID:130534062

USACE. (2021). *Coastal texas protection and restoration feasibility study* (tech. rep.). US Army Corps of Engineers. https://www.swg.usace.army.mil/Portals/26/Coastal%20TX%20Executive%20Summary_FINAL_20210827.pdf

Vader, H., Bakker, A. M. R., Jonkman, S. N., van den Boomen, M., van Baaren, E., & Diermanse, F. L. M. (2023). A framework for assessing the remaining life of storm surge barriers. *Structure and Infrastructure Engineering*, *20*(12), 2022–2034. https://doi.org/10.1080/15732479.2023.2177874

van Vledder, G., Hofland, B., Tuin, H., & van Maris, B. (2019). Numerical evaluation of design rules for non-breaking wave loads on vertical walls. In N. Goseberg & T. Schlurmann (Eds.), *Coastal structures 2019*. Bundesanstalt für Wasserbau. https://doi.org/10.18451/978-3-939230-64-9_076

Walraven, M., Vrolijk, K., & Kothuis, B. B. (2022a). Chapter 20 - design, maintain and operate movable storm surge barriers for flood risk reduction. In S. Brody, Y. Lee, & B. B. Kothuis (Eds.), *Coastal flood risk reduction* (pp. 271–286). Elsevier. https://doi.org/https://doi.org/10.1016/B978-0-323-85251-7.00020-2

Walraven, M., Vrolijk, K., & Kothuis, B. B. (2022b). Design, maintain and operate movable storm surge barriers for flood risk reduction. In S. Brody, Y. Lee, & B. B. Kothuis (Eds.), *Coastal flood risk reduction* (pp. 271–286). Elsevier. %5Curl%7Bhttps://doi.org/10.1016/B978-0-323-85251-7.00020-2%7D

Weller, H. G., Tabor, G., Jasak, H., & Fureby, C. (1998). A tensorial approach to computational continuum mechanics using object-oriented techniques. *Computer in Physics*, *12*(6), 620–631. https://doi.org/10.1063/1.168744

Yoshmi Goda, S. K. (1966). *Study on finate amplitude standing waves and their pressures upon a vertical wall* (tech. rep.). Institute ministry of transport Japan.

A

Appendix A

A.1. Bathymetry water level variations based on OpenFOAM and OceanWave3D

In this appendix, water elevation for the four wave gauges around the bathymetry variations is presented.

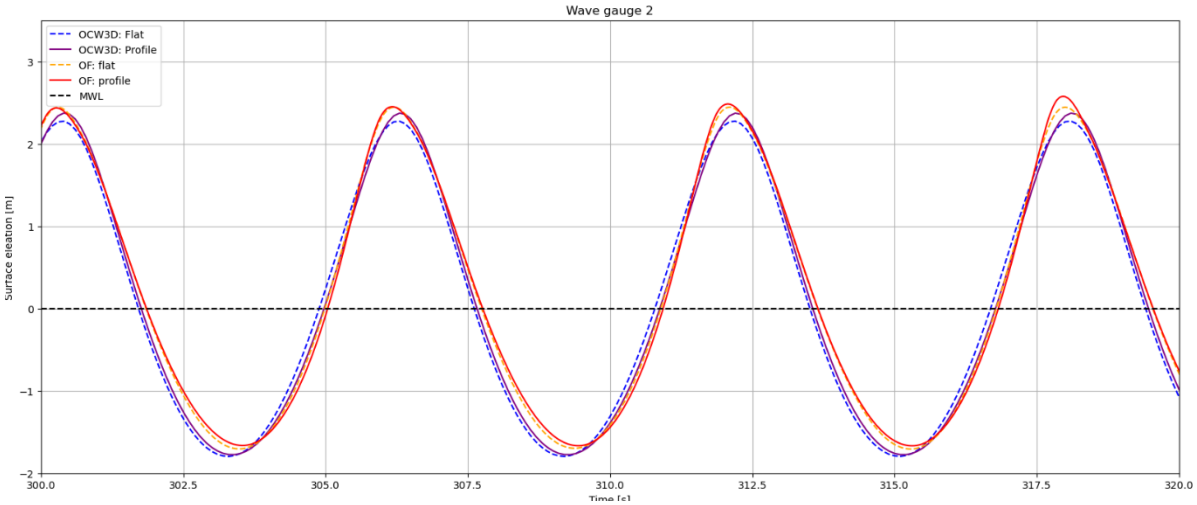

Figure A.1: Water level for t>300 at the wave gauge 2

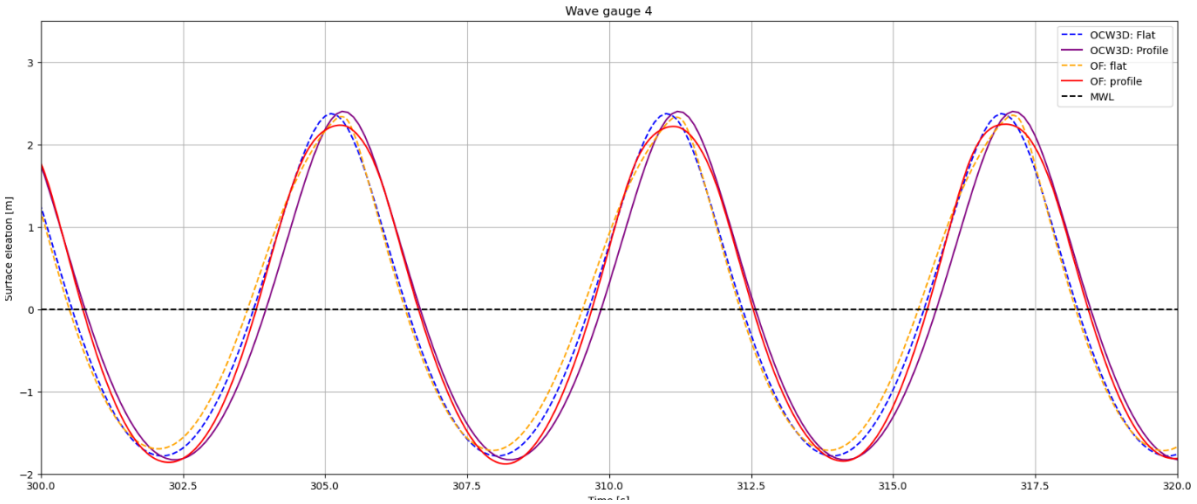

Figure A.2: Water level for t>300 at the wave gauge 4

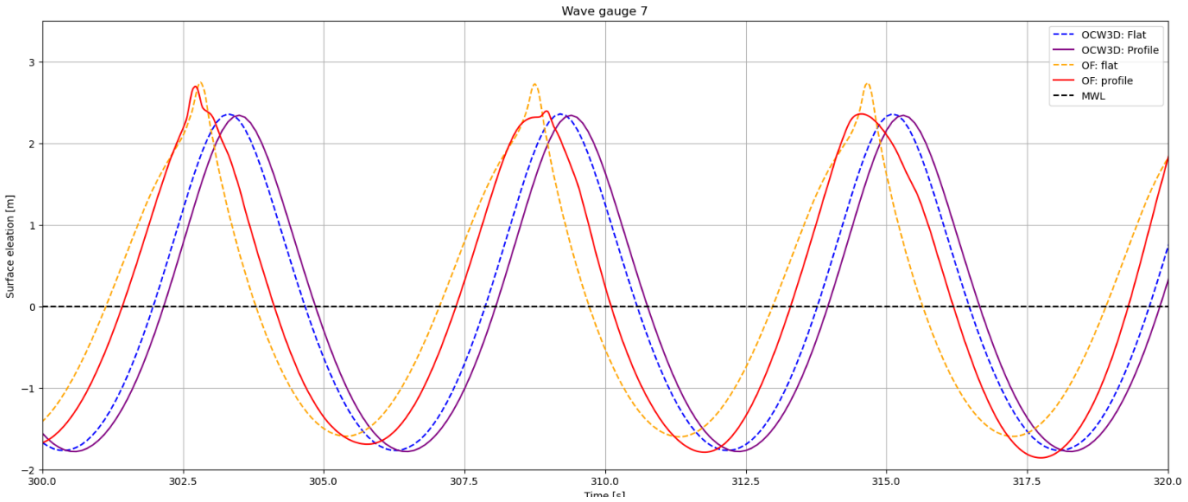

Figure A.3: Water level for t>300 at the wave gauge 7

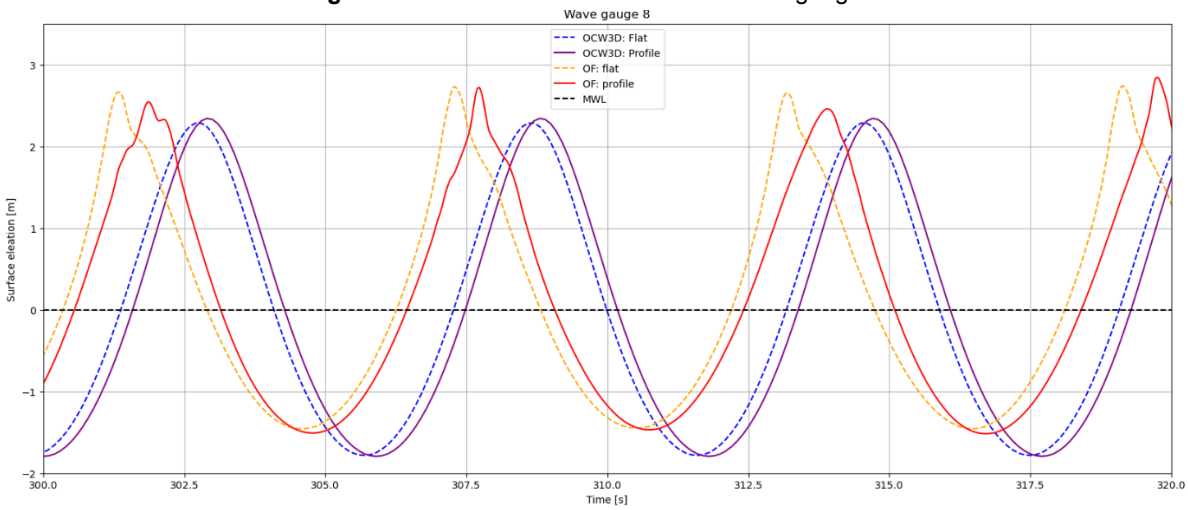

Figure A.4: Water level for t>300 at the wave gauge 8

B

Appendix B

B.1. Plotted force magnitude for antinodes of 3D pressure distributions and the phase differences

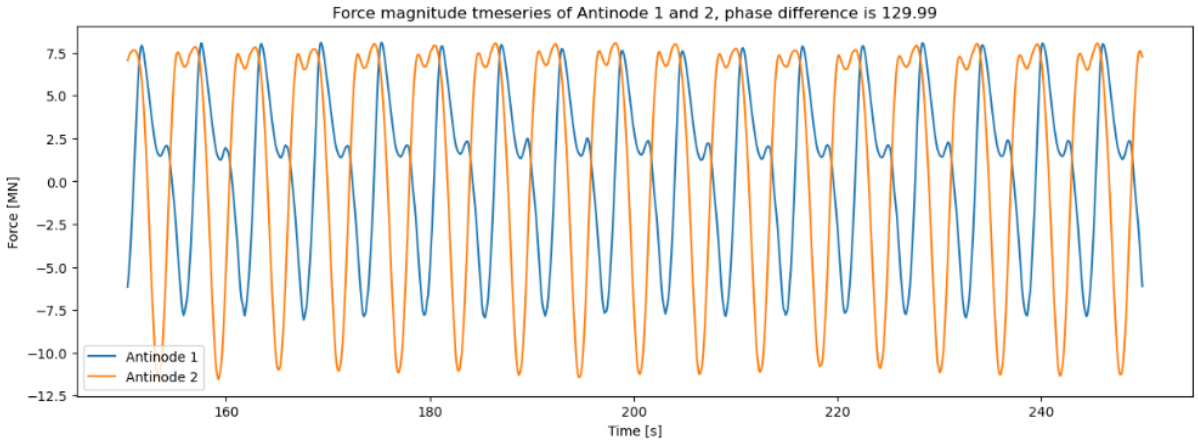

Figure B.1: Comparison of force magnitude timeseries for antinodes 1 and 2

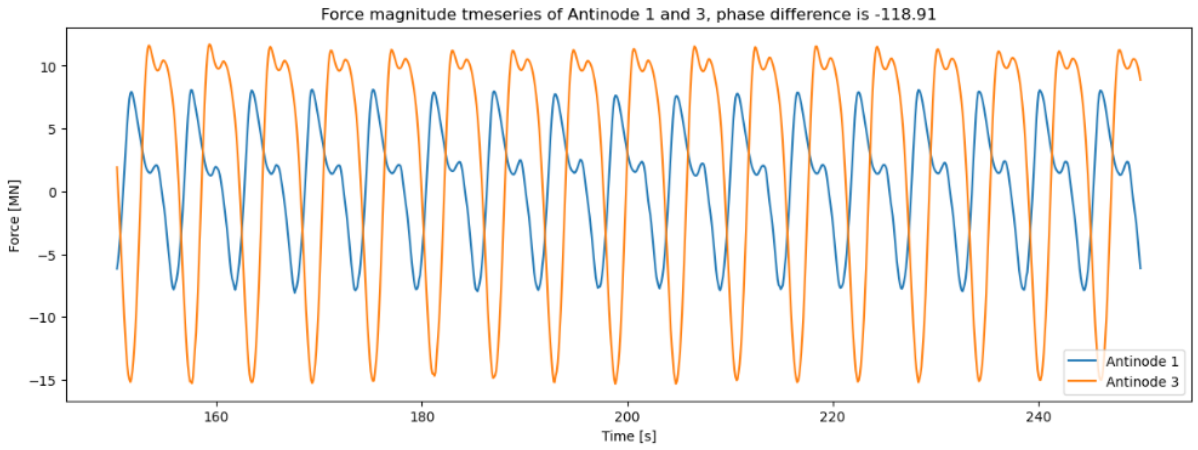

Figure B.2: Comparison of force magnitude timeseries for antinodes 1 and 3

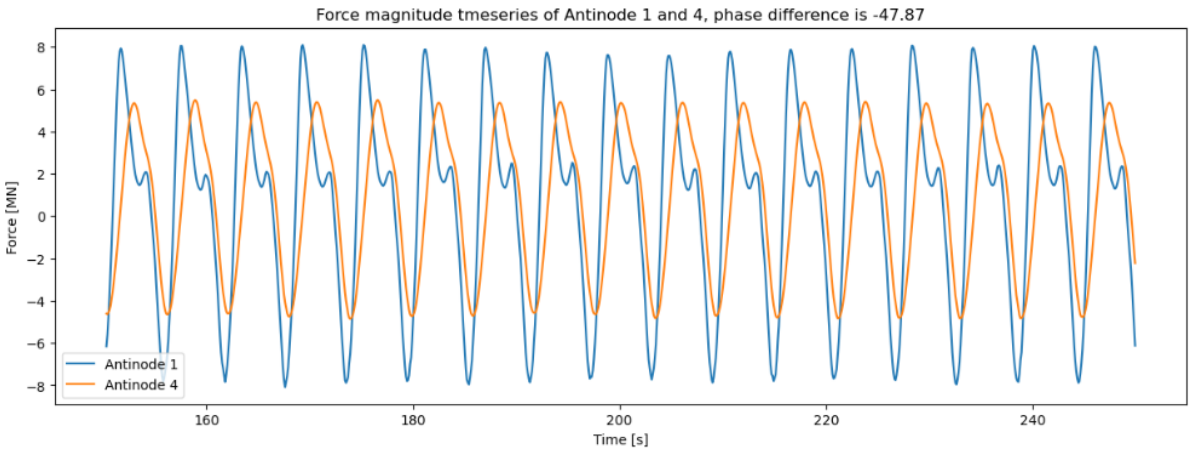

Figure B.3: Comparison of force magnitude timeseries for antinodes 1 and 4